Deformation of polycrystalline MgO at pressures of the lower mantle

Sébastien Merkel,[1,2] Hans Rudolf Wenk,[3] Jinfu Shu,[2] Guoyin Shen,[4] Philippe Gillet,[1] Ho-kwang Mao,[2] and Russell J. Hemley[2]

[1]   Room temperature investigations on the shear strength, elastic moduli, elastic anisotropy, and deformation mechanisms of MgO (periclase) are performed in situ up to pressures of 47 GPa using radial X-ray diffraction and the diamond anvil cell. The calculated elastic moduli are in agreement with previous Brillouin spectroscopy studies. The uniaxial stress component in the polycrystalline MgO sample is found to increase rapidly to 8.5($\pm$1) GPa at a pressure of 10($\pm$1) GPa in all experiments. Under axial compression, a strong cube texture develops which was recorded in situ. It is probable that the preferred orientation of MgO is due to deformation by slip. A comparison between the experimental textures and results from polycrystal plasticity suggest that the $\{110\}\langle 1\bar{1}0\rangle$ is the only significantly active slip system under very high confining pressure at room temperature. These data demonstrate the feasibility of analyzing elastic moduli, shear strength, and deformation mechanisms under pressures relevant for the Earth's lower mantle. Implications for the anisotropy and rheology of the lower mantle are discussed.   *INDEX TERMS:* 3909 Mineral Physics: Elasticity and anelasticity; 3924 Mineral Physics: High-pressure behavior; 5112 Physical Properties of Rocks: Microstructure; 5194 Physical Properties of Rocks: Instruments and techniques

1.   Introduction

[2]   Considerable progress has been made in establishing deformation mechanisms for minerals and rocks from the Earth's crust and upper mantle. Much of our knowledge about deformation of minerals such as halite, calcite, quartz, feldspars, and olivine relies on laboratory experiments on single crystals and rocks. It has been established that under a wide range of conditions minerals deform by dislocation glide and climb; in a polycrystalline rock, this leads to preferred orientation, which, in turn, leads to an anisotropic behavior, for example, for propagation of seismic waves. With the knowledge of deformation mechanisms we can understand and even model the development of anisotropy in the crust and the upper mantle [*Chastel et al.*, 1993]. However, much less is known about the deeper Earth, because pressures are beyond conditions reached by ordinary deformation devices such as the Griggs, Heard, or Paterson apparatus [see *Tullis and Tullis*, 1986].

[3]   While the pressure and temperature conditions are more extreme, the phases which are present in the lower mantle tend to have simpler crystal structures than minerals in the crust, as established by high-pressure experiments and theory (for a review, see *Fiquet* [2001]). Major phases in the lower mantle include $CaSiO_3$ perovskite, $(Mg,Fe)SiO_3$ silicate perovskite, $(Mg,Fe)O$ magnesiowüstite, and possibly SiO_2 stishovite. Very little is known about the deformation mechanisms of these phases at the conditions relevant to the Earth's mantle. This can be approached experimentally by studying analog materials that have the same structure but are stable at much lower pressure. For example, $CaTiO_3$ perovskite has been used as an analog for $MgSiO_3$ [*Karato and Li*, 1992; *Li et al.*, 1996], halite has been considered as an analog for magnesiowüstite and TiO_2 rutile for stishovite. Unfortunately the concept of analogs does not work very well for deformation mechanisms that depend on the local electronic structure around the dislocation core [e.g., *Poirier and Price*, 1999]. For example, slip systems of magnesite are entirely different than those of isostructural calcite. Halite has different slip systems than isostructural periclase or galena. In order obtain reliable results on deformation mechanisms that are active in the deep Earth, it is necessary to investigate the phases at prevailing pressure and temperature.

[4]   Diamond anvil cells allow experimental investigations over the whole pressure and temperature range of the lower mantle. They consist of different pressure steps and the degree of nonhydrostaticity of the stress conditions in the sample can be controlled by changing parameters such as the diamonds geometry or the pressure medium.

[1]Laboratoire des sciences de la Terre, École normale supérieure de Lyon, Lyon, France.
[2]Geophysical Laboratory, Carnegie Institution of Washington, Washington, District of Columbia, USA.
[3]Department of Earth and Planetary Science, University of California, Berkeley, California, USA.
[4]Consortium for Advanced Radiation Sources, University of Chicago and Advanced Photon Source, Argonne National Laboratory, Argonne, Illinois, USA.

Polycrystalline samples subjected to nonhydrostatic conditions in these experiments can develop preferred orientation. During such experiments the powder is first compacted and then plastically deformed by loading which has a directional stress component. While this is a detriment in the study of phase relations and equilibrium structures, it can become an advantage for investigating deformation at extreme pressure. This nonhydrostatic stress has been used to perform deformation experiments on lower mantle materials such as MgO [*Meade and Jeanloz*, 1988] or (Mg,Fe)SiO$_3$ perovskite [*Meade et al.*, 1995] but the texture analysis was performed on samples quenched to ambient pressure and temperature that were removed from the diamond anvil cell. In recent years, new experimental techniques, based on radial diffraction experiment, have been developed in order to study the influence of nonhydrostatic stress on the lattice strains of the sample, for example to deduce shear strength and single crystal elastic moduli [*Singh*, 1993; *Mao et al.*, 1996; *Singh et al.*, 1998b; *Mao et al.*, 1998; *Duffy et al.*, 1999a, 1999b; *Cynn and Yoo*, 2000; *Merkel et al.*, 2002]. In pilot experiments on iron at 54 and 220 GPa development of strong textures was observed and, based on the pattern, slip systems in hexagonal closed packed iron (ϵ-Fe) could be identified [*Wenk et al.*, 2000].

[5] In this study, the experimental technique has been further refined in order to study the shear strength, elastic moduli, and deformation mechanisms in greater detail. Our experiments were performed on a composite sample with iron powder embedded in MgO powder. In this report, we discuss the shear strength, single crystal elastic moduli, elastic anisotropy, and texture development in MgO from ambient pressure to 47 GPa at room temperature. We also describe the experimental technique and data reduction in some details. In a subsequent paper, we will discuss the texture development, including the bcc-hcp phase transition, and elastic properties of iron with increasing pressure.

[6] MgO is a simple oxide with the NaCl structure stable to high temperatures and megabar pressures [*Duffy et al.*, 1995; *Dewaele et al.*, 2000]. The P-V-T equation of state has been subject of numerous experimental and theoretical studies (see *Speziale et al.* [2001] for a review) and is well constrained over the pressure range (and part of the temperature range) of the lower mantle. Elastic moduli have been measured experimentally under ambient pressure up to 1800 K [*Isaak et al.*, 1989; *Sinogeikin et al.*, 2000], under ambient temperature up to 50 GPa [*Yoneda*, 1990; *Shen et al.*, 1998; *Reichmann et al.*, 1998; *Sinogeikin and Bass*, 2000; *Zha et al.*, 2000], and both pressure and temperatures of 8 GPa and 1600 K [*Chen et al.*, 1998]. Theoretical calculations of the moduli have been performed to lower mantle conditions [*Mehl et al.*, 1986; *Isaak et al.*, 1990; *Karki et al.*, 1997, 1999; *Stixrude*, 2000]. The shear strength of polycrystalline MgO has been studied at low pressures and high temperatures [*Paterson and Weaver*, 1970], ambient temperature and high pressures [*Bridgman*, 1937; *Kinsland and Bassett*, 1977; *Meade and Jeanloz*, 1988; *Duffy et al.*, 1995; *Uchida et al.*, 1996], and moderate pressures and high temperatures [*Weidner et al.*, 1994]. Deformation mechanisms have been examined under low pressure conditions [*Weaver and Paterson*, 1969; *Paterson and Weaver*, 1970], on quenched sample from high-pressure and ambient temperature diamond anvil cell experiments [*Meade and Jeanloz*, 1988], but no analysis was performed in situ under pressures relevant for the Earth's mantle. Recently some simple shear deformation experiments were performed on magnesiowüstite and texture patterns were used to identify deformation mechanisms [*Stretton et al.*, 2001]. We will compare those results with data for pure MgO in the discussion section. The motivation of this research is do develop methods for quantitative high-pressure deformation experiments at conditions corresponding to the lower mantle and inner core and investigate the ductile deformation, elastic behavior and shear strength of important deep mantle and core phases. We are starting with MgO but this experimental technique can be applied to a whole range of materials. In the first section of this paper we describe the high-pressure experimental techniques and the fundamentals of the data analysis we perform. We then present X-ray measurements and results for the uniaxial stress, single crystal elastic moduli and preferred orientation in the sample. Finally, we discuss the implications of these results for the shear strength of polycrystalline MgO, its deformation mechanisms under high pressure and ambient temperature, single-crystal elastic anisotropy, and implications for the anisotropy of the Earth's mantle.

2.   Experimental Details
2.1.   Experimental Technique

[7] High pressures and deformation of the sample were produced using a diamond anvil cell. Diamonds with a 300-μm tip diameter were chosen and a 65-μm hole drilled in the gasket to form a sample chamber. To allow diffraction in a direction orthogonal to the compression axis (Figure 1), the confining gasket was made of a mixture of amorphous boron and epoxy. The gasket thickness under the diamond tip was 80 μm at the beginning of the experiment. The samples were ground to a grain size of less than 1 μm to ensure a sufficient number of crystallites for reliable statistics in the analysis. The samples were pressed into platelets between two large diamonds (1000 μm tip diameter). In order to fill the sample chamber, a layer of MgO was deposited at the bottom of the gasket hole. Then, we added a small platelet of iron. Finally, another platelet of MgO was added above the Fe platelet and pressed with the diamond anvils. The geometry of the samples was slightly different between experiment 1 and 2. In experiment 2, the Fe platelet was well centered in the MgO powder during the whole experiment. In experiment 1, it moved while the cell was being closed and was not completely surrounded by the MgO powder.

[8] Diffraction experiments were conducted using angle-dispersive synchrotron X-ray diffraction techniques at the ID-13 beam line of the GSECARS sector at the Advanced Photon Source. The incident monochromatic X-ray beam of wavelength 0.4246 Å was focused to 10 μm × 6 μm. The size of the incident X-ray beam was measured using a sharp edge. Incoming and diffracted beam passed through the amorphous gasket that absorbed little of the X-ray beam; the diffraction patterns were collected using an imaging plate orthogonal to the incoming beam. The diamond anvil cell was oriented with the diamond axis perpendicular to the incoming X-ray beam (Figure 1).

[9] In order to locate the sample, we performed X-ray scans while moving the diamond cell in directions orthog-
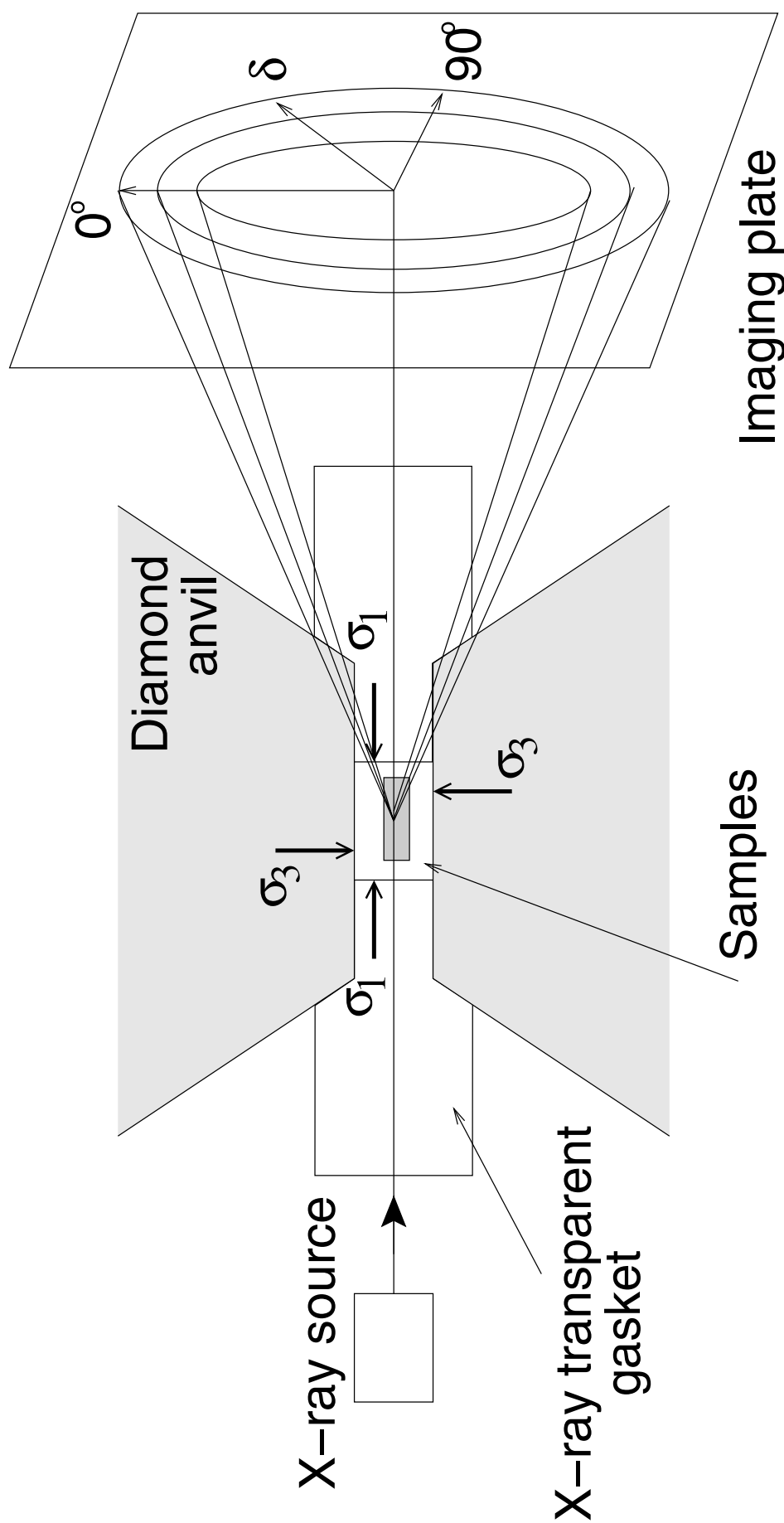
Figure 1. Schematic of the experiment. The polycrystalline sample is confined under nonhydrostatic stress conditions between the two diamond anvils. σ_3 is the axial stress imposed by the diamonds and σ_1 the radial stress imposed by the gasket. A monochromatic X-ray beam is sent through the gasket with the direction of the incoming beam orthogonal to the diamond axis and the data collected on an imaging plate orthogonal to the incoming beam. The position of the diffraction lines and intensity of diffraction are analyzed as a function of the azimuthal angle δ.
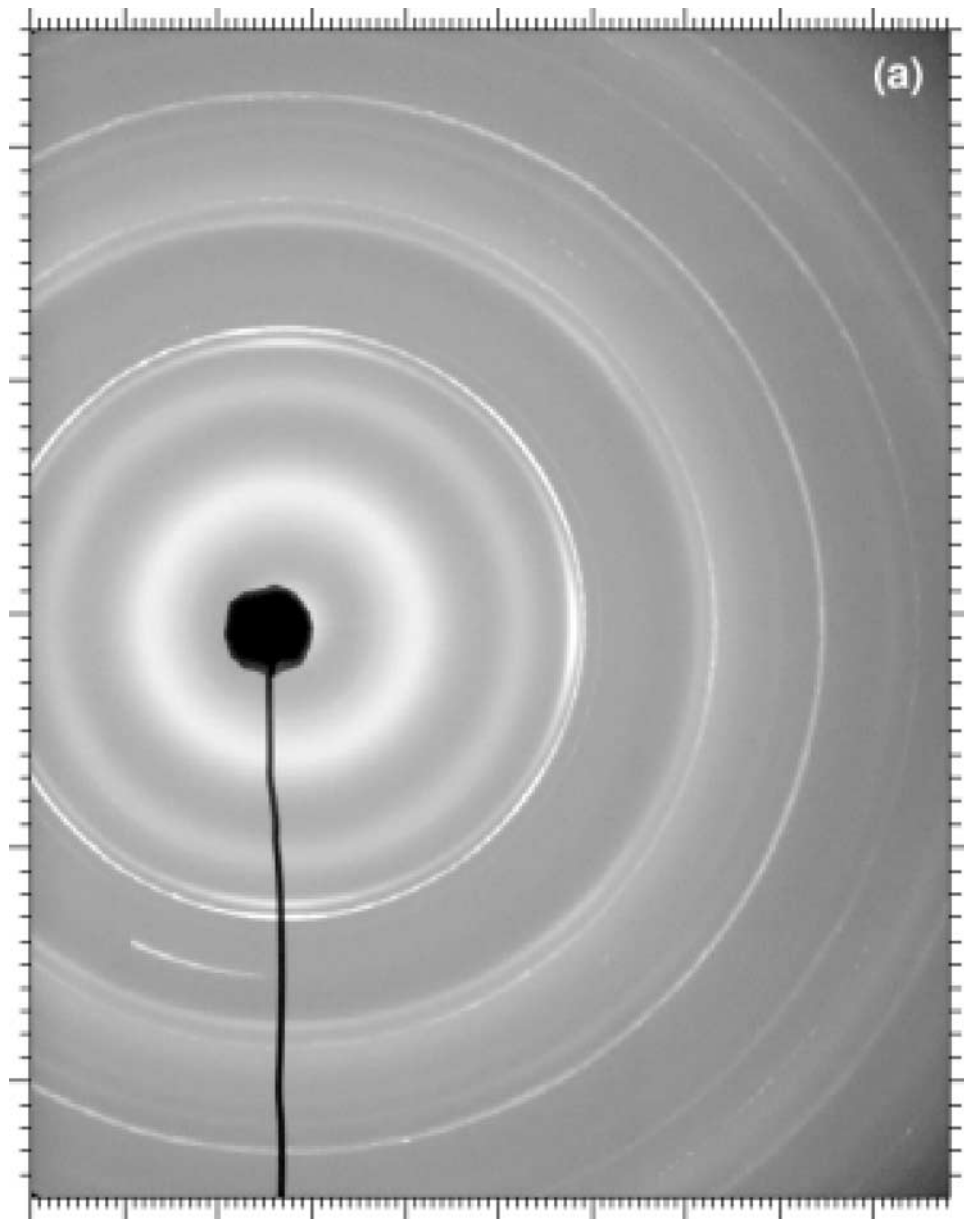
Figure 2. (a) Diffraction pattern at 9.5 GPa (experiment 1). (b) Representative spectra extracted from diffraction patterns from experiment 1 at 9.5 and 20.3 GPa for $\delta = -90°$, $-44°$, $0°$, $44°$, and $88°$ obtained with integrations over $2°$ intervals. Diffraction peaks for MgO, α-Fe ($P = 9.5$ GPa) and ϵ-Fe ($P = 20.3$ GPa) are labeled on the figure.

onal to the X-ray scans. The exact position of the sample was obtained by recording changes in the X-ray absorption. The result of these scans was then used to estimate the macroscopic size of the sample (thickness and width).

[10] Two sets of experiments were performed. Pressures in the first experiment ranged from 2 to 36 GPa. For experiment 2, patterns were recorded between 2 and 47 GPa on compression and 42 to 18 GPa on decompression. Each pattern took 7 to 10 min to record. Five diffraction peaks of MgO (111, 200, 220, 311, and 222) were used in the analysis. Equivalent hydrostatic pressures were measured according to the hydrostatic equation of state of MgO [*Speziale et al.*, 2001] after correcting the data for effects of nonhydrostatic stress [*Singh et al.*, 1998a]. In all cases, the

pressures inferred from Fe do not differ from those deduced from MgO by more than 2 GPa.

2.2. Data Reduction

[11] The image plate diffraction data are analyzed with FIT2D [*Hammersley*, 1998]. Figure 2a shows an example of a measured diffraction spectrum. The variation of the diffraction intensity along the diffraction rings yields information about the orientations of the lattice planes and thus plastic strains, while the variation of the position of the diffraction peak along the rings is related to elastic properties of the sample. The imaging plate azimuthal angle δ is chosen to be zero when the diamond axis is in the plane defined by the diffracted and incoming beams
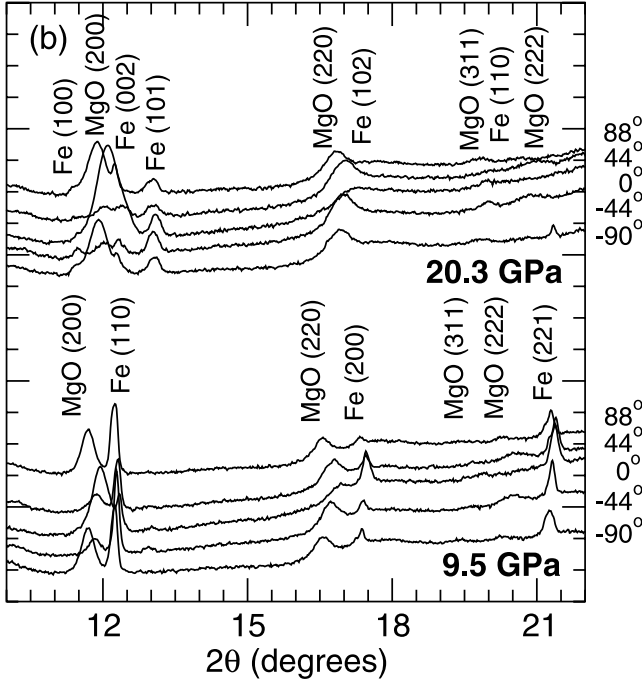
Figure 2. (continued)

component (a measure of the deviatory stress). Because of the nonhydrostatic stress, the observed d-spacings depend on the angle χ between the diffracting plane normal and the load axis (Figure 3).

[15] Variation of the d-spacings with χ, stress conditions in the sample and their relation to the uniaxial stress component, shear strength, and the elastic moduli of MgO were analyzed using the theory described by *Singh* [1993] and *Singh et al.* [1998a]. It relates the macroscopic strain and microscopic single crystal elastic moduli assuming a randomly textured sample under the Reuss-Voigt-Hill average [*Matthies et al.*, 2001] and has been successfully applied to other cubic symmetry materials under high pressure such as pyrite [*Merkel et al.*, 2002], gold and molybdenum [*Duffy et al.*, 1999b] and tantalum [*Cynn and Yoo*, 2000]. Other determinations of the single-crystal elastic moduli from diffraction experiments on polycrystals include copper, steel or aluminum at ambient pressure by X-ray diffraction [*Ganäupel-Herold et al.*, 1998], Ni-Cr-Fe alloy, hexagonal Ti, cubic zirconia, tetragonal zirconia under ambient pressure by neutron diffraction [*Howard and Kisi*, 1999], and ϵ-Fe up to 220 GPa by radial X-ray diffraction [*Mao et al.*, 1998]. The details of this analysis have been described elsewhere [*Singh*, 1993; *Singh et al.*,
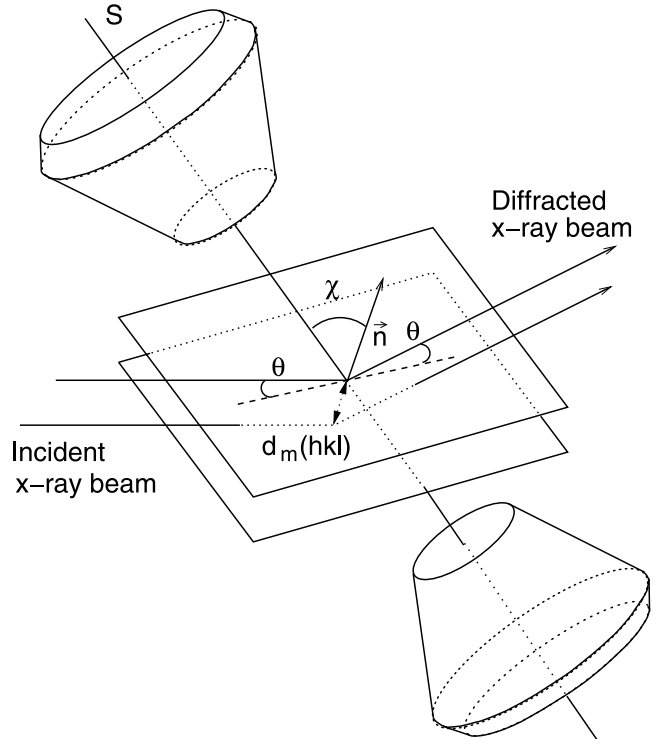
(Figure 1). The raw image was corrected for distortion using a CeO$_2$*xdvi* standard.

[12] In order to study the variations in the position of the diffraction peaks and their intensity with the azimuthal angle δ, the diffraction patterns are cut into small arcs of 2° to 4° and integrated with FIT2D. For each pattern, this produces between 55 and 110 segments with the diffraction intensity as a function of the diffraction angle 2θ for δ between −110° and 110°. Figure 2b presents some representative spectra from experiment 1 at 9.0 and 20.3 GPa, for δ = −90°, −44°, 0°, 44°, and 88° obtained with integrations over 2° intervals. Diffraction peaks for MgO and Fe are labeled on the figure.

[13] The patterns are then fitted individually assuming Gaussian peak profiles and a linear local background. The pole distance χ, which corresponds to the angle between the diffracting plane normal and the load axis (Figure 3), is calculated from

$$\cos \chi = \cos \theta \cos \delta, \tag{1}$$

where θ is the diffraction angle.

2.3. Uniaxial Stress and Elasticity Analysis

[14] Because of the symmetry of the experiment (Figure 1), the stress conditions in the sample can be described as

$$\sigma = \begin{bmatrix} \sigma_1 & 0 & 0 \\ 0 & \sigma_1 & 0 \\ 0 & 0 & \sigma_3 \end{bmatrix} = \begin{bmatrix} \sigma_P & 0 & 0 \\ 0 & \sigma_P & 0 \\ 0 & 0 & \sigma_P \end{bmatrix} + \begin{bmatrix} -\frac{t}{3} & 0 & 0 \\ 0 & -\frac{t}{3} & 0 \\ 0 & 0 & 2\frac{t}{3} \end{bmatrix},$$

$$\tag{2}$$

where σ_1 and σ_3 are the radial and axial stress components, respectively; σ_P is the normal mean stress or equivalent hydrostatic pressure, and $t = (\sigma_3 - \sigma_1)$ is the uniaxial stress

Figure 3. Geometry of the diffraction for a given χ angle between the diffracting plane normal $\vec{n}$ and the maximum stress axis S, we measure a d-spacing $d_m(hkl)$ function of the Miller indices h, k, and l, but also the angle χ because of the nonhydrostatic compression. When $\chi = 0°$, the diffracting plane is orthogonal with the maximum stress axis S, thus $d_m(hkl)$ is minimum. When $\chi = 90°$, the diffracting plane is aligned with the maximum stress axis S, thus $d_m(hkl)$ is maximum.

1998a]. We present here a short summary of the main features.

[16] The d-spacings for a given set of lattice planes measured by X-ray diffraction is a function of the angle χ between the principal stress axis of the diamond cell and the diffracting plane normal (see Figure 3) and can be expressed as:

$$d_m(hkl) = d_P(hkl)[1 + (1 - 3\cos^2\chi)Q(hkl)], \qquad (3)$$

where $d_m(hkl)$ is the measured d-spacing and $d_P(hkl)$ the d-spacing under the hydrostatic pressure σ_P. $Q(hkl)$ is given by

$$Q(hkl) = \frac{t}{3}\left[\frac{\alpha}{2\,G_R(hkl)} + \frac{1-\alpha}{2\,G_V}\right]. \qquad (4)$$

$G_R(hkl)$ and $G_V(hkl)$ are the shear moduli of the aggregate under the Reuss (iso-stress) and Voigt (iso-strain) approximations, respectively, and are not orientation dependent. The factor α, which lies between 0 and 1, determines the relative weight of isostress (Reuss) and isostrain (Voigt) conditions. It specifies the degree of stress and strain continuity across grains in the sample.

[17] For a cubic system, we have

$$(2\,G_V)^{-1} = \frac{5}{2}\frac{(S_{11} - S_{12})S_{44}}{[3(S_{11} - S_{12}) + S_{44}]} \qquad (5)$$

and

$$(2\,G_R)^{-1} = S_{11} - S_{12} - 3\,S\,\Gamma(hkl), \qquad (6)$$

where

$$S = S_{11} - S_{12} - S_{44}/2 \qquad (7)$$

and

$$\Gamma(hkl) = \frac{h^2k^2 + k^2l^2 + l^2h^2}{(h^2 + k^2 + l^2)^2}. \qquad (8)$$

The S_{ij} are the single crystal elastic compliances; S is a measure of elastic anisotropy.

[18] According to equation (3), $d_m(hkl)$ should vary linearly with $(1 - 3\cos^2\chi)$. The intercept ($\chi = 54.7°$) yields $d_P(hkl)$, the d-spacing due to the hydrostatic component of the stress, and the slope the product $d_P(hkl)Q(hkl)$.

[19] Equations (4)–(6) imply a linear relationship between $Q(hkl)$ and $3\Gamma(hkl)$ with intercept m_0 and slope m_1 given by

$$m_0 = \frac{t}{3}\left[\alpha(S_{11} - S_{12}) + (1 - \alpha)\frac{5}{2}\frac{(S_{11} - S_{12})S_{44}}{[3(S_{11} - S_{12}) + S_{44}]}\right] \qquad (9)$$

$$m_1 = -\frac{\alpha t}{3}[S_{11} - S_{12} - S_{44}/2]. \qquad (10)$$

[20] The bulk modulus K is defined by

$$K_T = -V\left(\frac{\partial p}{\partial V}\right)_T = \frac{1}{3[S_{11} + 2\,S_{12}]}. \qquad (11)$$

The uniaxial stress component in the sample t is estimated with the relation

$$t = 6G\langle Q(hkl)\rangle, \qquad (12)$$

where G is the shear modulus of the aggregate.

[21] Deducing m_0 and m_1 from the experimental data, using the bulk modulus calculated from an equation of state, and estimating the uniaxial stress t, we have enough information to deduce the three elastic compliances S_{11}, S_{12}, and S_{44} of a cubic material that can be inverted to the three independent elastic stiffnesses C_{11}, C_{12}, and C_{44}.

[22] The bulk modulus and its variation with pressure is calculated using a third-order finite strain equation

$$K_T = (1 + 2f)^{5/2}[k_0 + k_1 f], \qquad (13)$$

where

$$k_0 = K_{0T}$$
$$k_1 = 3K_{0T}K'_{0T} - 5K_{0T}, \qquad (14)$$

The Eulerian strain f is given by

$$f = \frac{1}{2}\left[\left(\frac{\rho}{\rho_0}\right)^{2/3} - 1\right]. \qquad (15)$$

For the shear modulus, it is necessary to use a fourth-order finite-strain equation [*Davies and Dziewonski*, 1975; *Duffy and Ahrens*, 1992]

$$G_T = (1 + 2f)^{5/2}[g_0 + g_1 f + g_2 f^2], \qquad (16)$$

where

$$g_0 = G_{0T}$$
$$g_1 = 3K_{0T}G'_{0T} - 5G_{0T}$$
$$g_2 = \frac{9}{2}\left[K_{0T}^2\left(G''_{0T} + (K'_{0T} - 4)\frac{G'_{0T}}{K_{0T}}\right) + \frac{35G_{0T}}{9}\right]. \qquad (17)$$

[23] For MgO, we calibrate our analysis with the bulk and shear moduli obtained from Brillouin spectroscopy up to 50 GPa [*Zha et al.*, 2000] and first principles calculation at 300 K [*Karki et al.*, 1999]. Differences between isothermal and adiabatic parameters are defined by

$$\frac{K_S}{K_T} = 1 + \alpha\gamma T, \qquad (18)$$

where the subsequent T and S refer to isothermal and adiabatic. For MgO, we use $\alpha_0 = 1.5 * 10^{-5}\mathrm{K}^{-1}$ and $\gamma_0 = 1.52$ [*Speziale et al.*, 2001]; thus, differences between adiabatic and isothermal parameters are on the order of 1.5% and are neglected in this study. Numerical values fitted to results from Brillouin spectroscopy and 300 K first-principles calculations are given in Table 1. The parameters used are in agreement with numerous high pressure and high temperature equation of state measurements (for a review, see *Speziale et al.* [2001]).

2.4. Preferred Orientation Analysis

[24] Because of the application of nonhydrostatic stress, the polycrystalline MgO, after compaction, undergoes ductile deformation and strong lattice preferred orientation is produced. The texture in the sample can be represented by the orientation distribution function (ODF) which is a probability function for finding an orientation and it is normalized such

Table 1. Finite Strain Parameters Used to Scale This Analysis[a]

	Brillouin	First Principles
K_0, GPa	162.5	162
K_0'	3.99	4.15
G, GPa	130.4	128
G_0', GPa	2.89	2.90
G_0'', GPa^{-1}	−0.084	−0.042

[a] They were fitted to results from Brillouin spectroscopy [*Zha et al.*, 2000] between 0 and 50 GPa and first principles calculations [*Karki et al.*, 1999] at 300 K and between 0 and 100 GPa.

that the integral over the whole orientation space is unity. An aggregate with a random orientation distribution has a probability of one for all orientations, or one multiple of a random distribution (m.r.d.). If preferred orientation is present, some orientations have probabilities higher than one and others lower than one [*Kocks et al.*, 1998].

[25] For each orientation g, the ODF $f(g)$ describes the probability density of finding crystallites that have the orientation g within dg. We have

$$f(g) > 0; \quad \int_G f(g)d\overline{g} = 1 \text{ where } d\overline{g} = \frac{1}{8\pi^2}dg. \quad (19)$$

The degree of anisotropy in the sample is expressed by the texture sharpness F_2 defined as

$$F_2 = \int_G [f(g)]^2 d\overline{g}. \quad (20)$$

For a material with random texture, the texture sharpness F_2 is equal to 1, for a textured material $F_2 > 1$.

[26] The analysis of the diffraction intensities to deduce the ODF is similar to that of *Heidelbach et al.* [1999] and *Wenk et al.* [2000]. Because of the axial symmetry of the stress conditions in the experiment (Figure 1 and equation (2)), it is sufficient to study the variation of the diffraction intensities with angle χ between the diffracting plane normal and the diamond axis in order to deduce the full ODF of the sample. The angle χ is related to the azimuth angle δ on the imaging plate by equation (1). Thus there is a blind region and orientations with $|\chi| < \theta$ cannot be probed in the experiment. The incomplete pole figures obtained from the measurements are nevertheless sufficient for calculating the three-dimensional ODF.

3. Results

3.1. Macroscopic and Microscopic Deformation

[27] Figure 4 shows the distance between the diamond anvils we deduce from the X-ray scans as a function of pressure for the two experiments. Upon compression, this is a good estimation of the macroscopic sample thickness. However, upon decompression, these quantities differ as the sample is not put into extension. The process can be divided into three sections. First, we observe a compaction of the sample powder due to the fact that the sample chamber was not fully filled with sample at the start of the experiment. The thickness varies greatly without any large pressure increase. Later the sample deforms regularly and the macroscopic strain of the sample reaches the order of 200%. This region is where we expect to see the texture developing.

Above 15 GPa, the resolution of the X-ray scans does not allow us to observe any change in the thickness.

[28] Figure 5 presents the variation of d-spacing of the (200) line of MgO with $(1 - 3 \cos^2 \chi)$ for experiment 2 and selected pressures, where χ is the pole figure distance. Assuming a Reuss-Voigt-Hill micromechanical model and a sample with randomly oriented grains, a linear relationship is expected (section 2.3). Deviations between the linear fits and the data are due to intrinsic experimental errors and effects of texture on the lattice strains. These deviations cannot be resolved on these figures.

[29] Assuming a random texture and using the Reuss-Voigt-Hill approximation, the d-spacings at $\chi = 57.4°$ correspond to the crystal unit cell under equivalent hydrostatic pressure (section 2.3). These were used to calibrate the pressure in the experiment with a previously measured hydrostatic equation of state [*Speziale et al.*, 2001].

3.2. Uniaxial Stress

[30] Using the least squares fits of the data from Figure 5, the shear modulus obtained from Brillouin spectroscopy or first-principle calculations (Table 1), we can evaluate the uniaxial stress component $t = \sigma_3 - \sigma_1$ in the sample (section 2.3). Figure 6 shows the evolution of t for experiments 1 and 2. In experiment 1, we see a sharp increase of t from 0 to 7 GPa between ambient pressure and 10 GPa. Above 10 GPa, the uniaxial stress component in the MgO sample remains approximately constant at 8 GPa. In experiment 2 (Figure 6b), t is better resolved and its behavior more
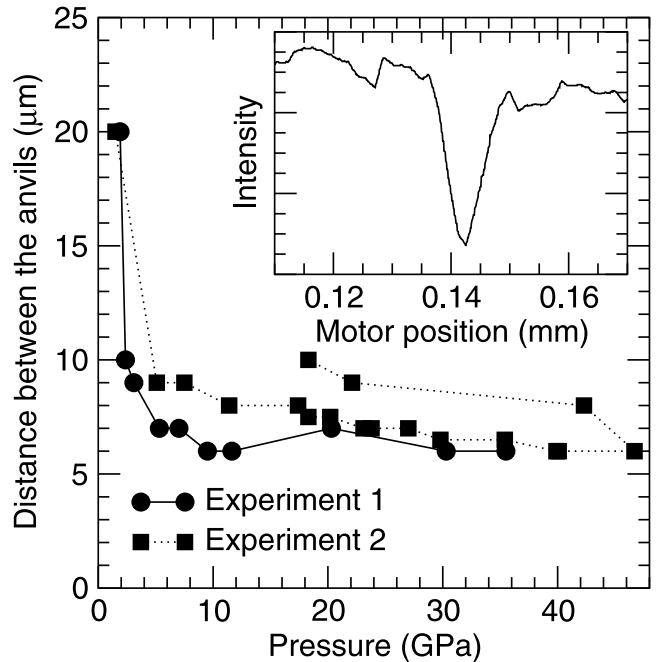

Figure 4. Distance between the diamond anvils as a function of pressure. Upon compression this is a good estimation of the sample thickness. However, upon decompression these quantities differ as the sample is not put into extension. In the inset we show an example of transmitted X-ray intensity measured while moving the diamond anvil cell perpendicular to the incoming beam that is used to deduce the sample thickness for experiment 1 at 7 GPa.
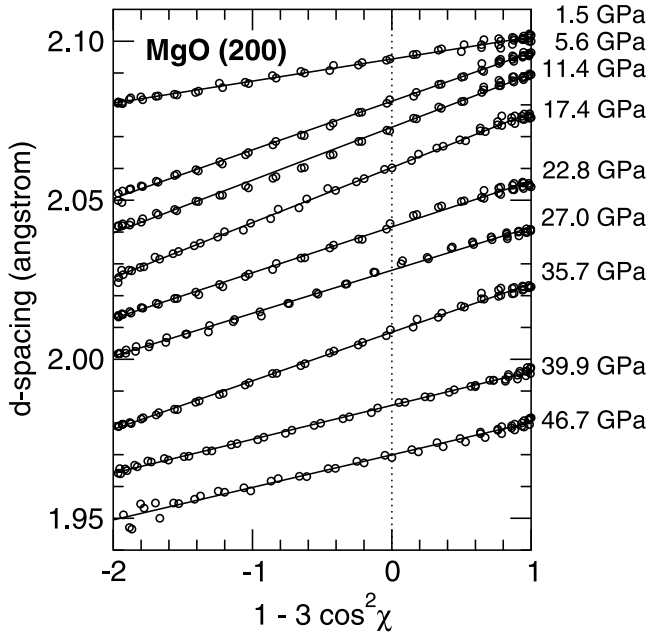
Figure 5. Variation of the *d*-spacing of the MgO (200) plane with $(1 - 3 \cos^2 \chi)$ where χ is the pole distance for selected pressures of experiment 2. The dotted line indicates the angle $\chi = 57.4°$ where, under a Reuss-Voigt-Hill and no texture approximation, the measured *d*-spacing corresponds to the unit cell under equivalent hydrostatic pressure. Solid lines are linear least squares fits through the data.

complicated. With the phase transition of the companion Fe sample from the α-phase to the ϵ phase around 12 GPa, we observe a decrease of the uniaxial stress component within the MgO sample. This can be explained by the decrease in

unit cell volume associated to the phase transition of iron which created a release of the stresses in the whole sample chamber. The companion Fe sample was heated using a YAG laser three times along the pressure increase, at 30, 35, and 40 GPa. We estimate that the temperature in Fe reached approximately 1200 K. However, this temperature is too low to allow precise measurement using the spectral radiometry techniques [*Heinz and Jeanloz*, 1987]. After heating, the MgO diffraction peaks remained very intense. Even though the iron might have reacted with the surrounding MgO powder, the amount of MgO present in the cell was still very important and we do not think it affected the data presented here. In all cases, the heating of the Fe sample released the stresses in the sample chamber, decreasing the uniaxial stress component in MgO.

3.3. Calculation of Elastic Moduli

[31] Assuming a random texture and a Reuss-Voigt-Hill micromechanical model, the single crystal elastic moduli can also be calculated from the fits in Figure 5 (section 2.3). The stress conditions in the sample, equivalent hydrostatic pressure and uniaxial stress, have to be precisely calibrated. Figure 7 presents the elastic moduli we obtained from experiment 1 using pressures deduced from the hydrostatic EOS of MgO [*Speziale et al.*, 2001] and uniaxial stress values from Figure 6 for $\alpha = 1$ (Reuss bound) and $\alpha = 0.5$ (Hill average) along with results from Brillouin spectroscopy [*Zha et al.*, 2000] and 300 K first principles calculations [*Karki et al.*, 1999].

[32] At low pressures, results from first principles calculations and Brillouin spectroscopy are not distinguishable and the Reuss average provides a better agreement for our results. It appears that the use of linear elasticity theory (section 2.3) still holds even though the uniaxial stress *t* is
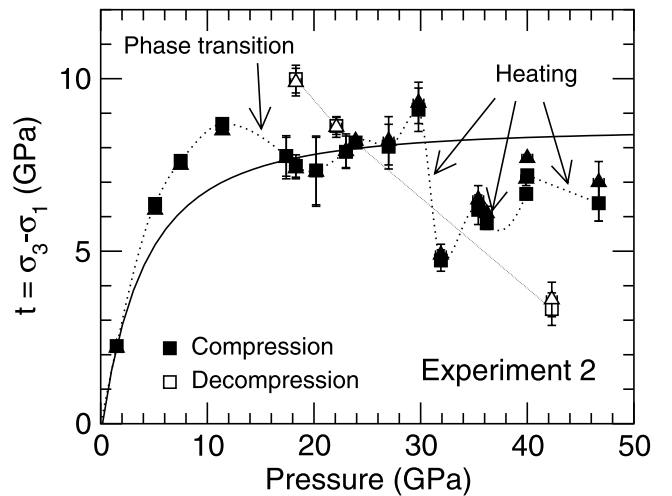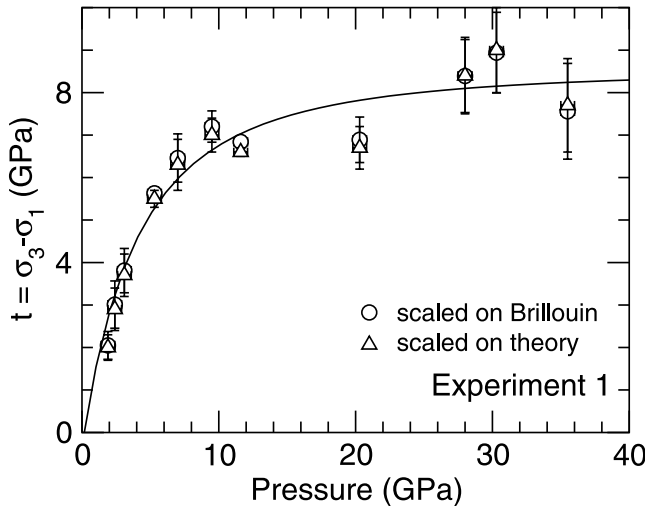

Figure 6. Uniaxial stress component in the MgO sample. (a) Uniaxial stress component in MgO upon compression for experiment 1 calculated using shear moduli from Brillouin spectroscopy (open squares) or first principles calculations (open triangles) (see Table 1). Solid line is a fit to the data. (b) Uniaxial stress component in MgO upon compression (solid symbols) and decompression (open symbols) for experiment 2 calculated using shear moduli from Brillouin spectroscopy (squares) or 300 K first principles calculations (triangles). Solid line is the fit from experiment 1, and dotted line a guide to the eye based on results scaled on Brillouin data. Operations performed on the Fe in contact with the MgO (phase transition, laser heating) are labeled.
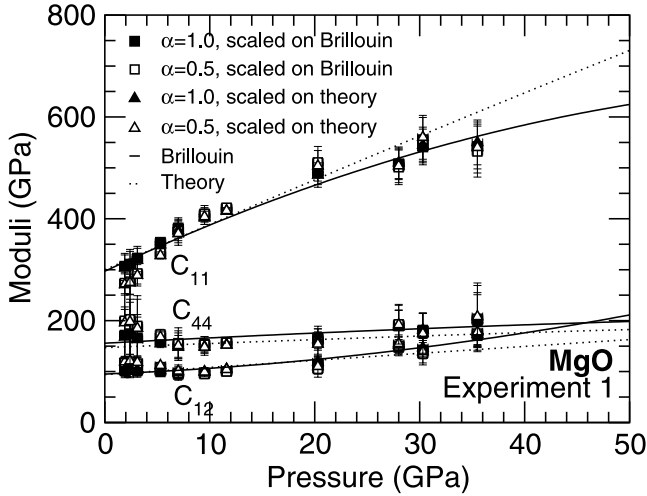
Figure 7. Elastic moduli of MgO calculated for experiment 1 assuming no texture in the sample We used both the Reuss bound (α =1, solid symbols) and Hill-average (α = 0.5, open symbols), and scaled the calculations on results from Brillouin spectroscopy from (squares) or 300 K first-principles calculations (triangles) (see Table 1). Solid and dotted lines show elastic moduli from Brillouin spectroscopy.

very large compared to the pressure. At higher pressures, results from the Reuss and Hill averages are very similar. This is due to the drop of elastic anisotropy of MgO (see section 4.4). m_1 in the lattice strains equations (equation (9)) is close to zero. Therefore we have a direct relation between ($C_{11} - C_{12}$) and C_{44} and the calculated elastic moduli do not depend on α. However, results from Brillouin spectroscopy and 300 K first-principles calculations diverge and our
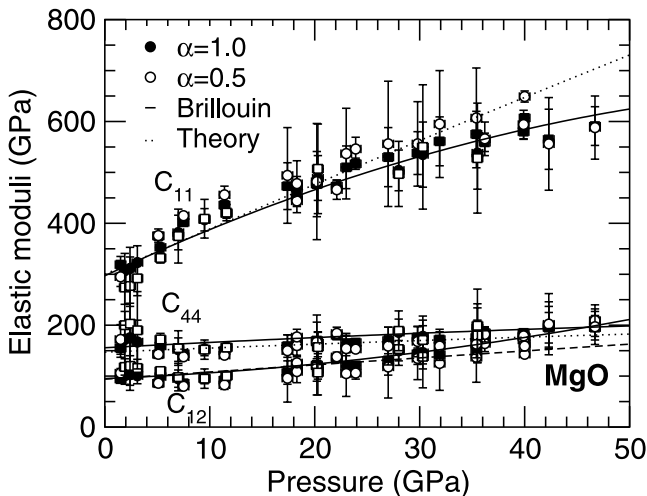

Figure 8. Elastic moduli of MgO calculated assuming no texture in the sample and using the Reuss bound (closed symbols) or Hill-average (open symbols) for experiment 1 and 2 and scaled on Brillouin spectroscopy (Table 1). Circles and squares are results from experiment 1 and 2, respectively. Solid and dotted lines are fits to results from Brillouin spectroscopy.

measurements are in better agreement with the elastic moduli from Brillouin spectroscopy.

[33] Figure 8 and Table 2 present the elastic moduli of MgO from experiment 1 and 2 calculated under the Reuss or Hill approximation with uniaxial stress values scaled on Brillouin spectroscopy along with the results from Brillouin spectroscopy and 300 K first-principles calculations. The good agreement between the results of the two experimental methods proves the utility of the lattice strain analysis for determining elastic moduli using X-ray diffraction for materials with cubic symmetry. The very large degree of preferred orientations in the sample does not appear to have a great influence on the calculations. A critical step in the analysis is to constrain the exact stress conditions (pressure and uniaxial stress) in the sample.

3.4. Preferred Orientation

[34] Figure 9 presents the intensities of diffraction for MgO (200) and MgO (220) as a function of the angle χ between the diffraction plane normal and the diamonds axis for all increasing pressures in the first experiment. At 1.90 GPa we do not see any preferred orientation. The variation of the intensity of diffraction with χ is the same for both peaks (200) and (220). We deduce that this intensity variation is created by our experimental setup and this is used as a background correction for all other analyses. Above 1.90 GPa, we observe the progressive development of a sharp texture in the sample. The (200) peak exhibits a maximum of intensity of diffraction at $\chi = 0°$ and $\chi = 90°$, meaning that the $\langle 100 \rangle$ axis of the sides of the crystallites

Table 2. Uniaxial Stress and Single Crystal Elastic Moduli of MgO as a Function of Pressure for Experiments 1 and 2[a]

Experiment	P	$\sigma(P)$	t	$\sigma(t)$	C_{11}	$\sigma(C_{11})$	C_{12}	$\sigma(C_{12})$	C_{44}	$\sigma(C_{44})$
1	1.9	0.5	2.0	0.3	307	34	101	17	172	55
1	2.4	0.5	3.0	0.6	311	42	103	21	175	68
1	3.1	0.5	3.8	0.5	323	33	101	16	167	43
1	5.3	0.5	5.6	0.2	353	8	99	4	159	7
1	7.0	0.5	6.5	0.6	382	34	95	17	152	23
1	9.5	0.5	7.2	0.3	407	22	96	11	153	13
1	11.6	0.5	6.8	0.1	419	9	101	5	157	5
1	20.3	0.5	6.9	0.5	489	44	116	22	165	21
1	30.3	0.5	8.9	0.9	535	64	146	32	178	32
1	35.5	0.5	7.4	1.1	538	71	175	35	194	48
2	1.5	0.5	2.2	0.1	319	16	94	8	155	18
2	5.1	0.5	6.4	0.1	375	7	86	4	143	4
2	7.5	0.5	7.6	0.1	402	1	86	1	144	1
2	11.4	0.5	8.7	0.1	436	8	92	4	150	4
2	17.4	0.5	7.7	0.6	473	46	107	23	159	22
2	18.3	0.5	7.4	0.3	468	24	114	12	165	13
2	20.2	0.5	7.3	1.0	477	64	122	32	170	36
2	23.0	0.5	7.8	0.5	510	42	119	21	165	19
2	23.9	0.5	8.1	0.1	517	11	121	5	166	5
2	27.0	0.5	7.9	0.6	530	58	131	29	170	26
2	29.8	0.5	9.0	0.6	538	42	144	21	176	21
2	31.9	0.5	4.6	0.3	561	48	142	24	172	20
2	35.4	0.5	6.1	0.4	575	45	153	23	176	20
2	36.2	0.5	5.7	0.2	559	18	168	9	185	10
2	39.9	0.5	6.5	0.2	580	15	177	7	185	8
2	40.0	0.5	7.0	0.1	607	5	164	2	176	2
2	46.7	0.5	6.2	0.5	591	38	208	19	195	24
2	42.3	0.5	3.2	0.5	565	59	195	30	197	40
2	22.1	0.5	8.6	0.2	473	12	134	6	180	8
2	18.3	0.5	9.9	0.4	451	15	123	7	173	10

[a] Values were calculated using the Reuss bound and scaled on Brillouin spectroscopy (Table 1). Pressures, uniaxial stresses, moduli, and standard deviations are given in GPa.
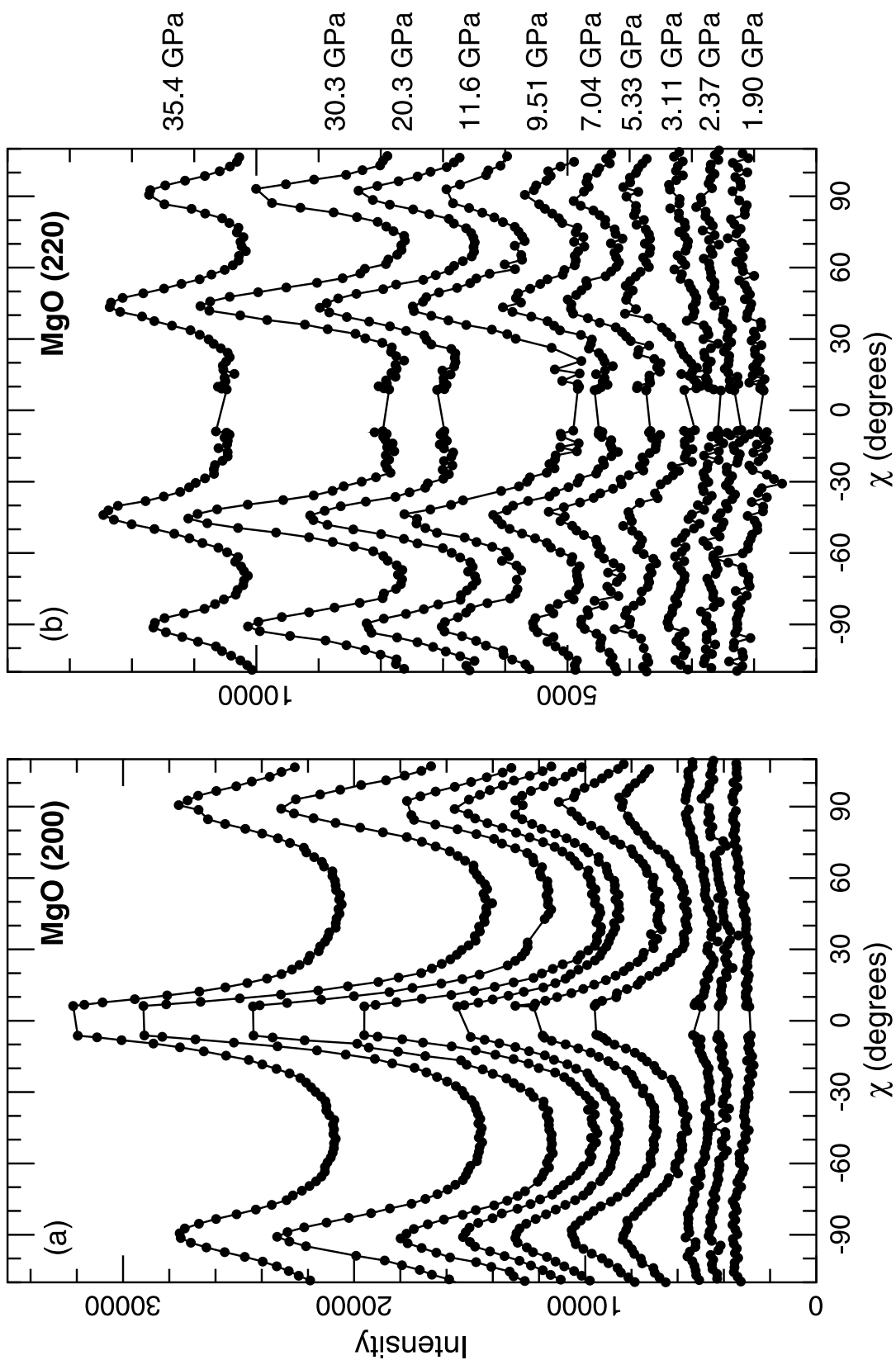
Figure 9. Intensity of diffraction as a function of the pole distance χ for MgO (200) (a) and MgO (220) (b) for all increasing pressures in experiment 1.
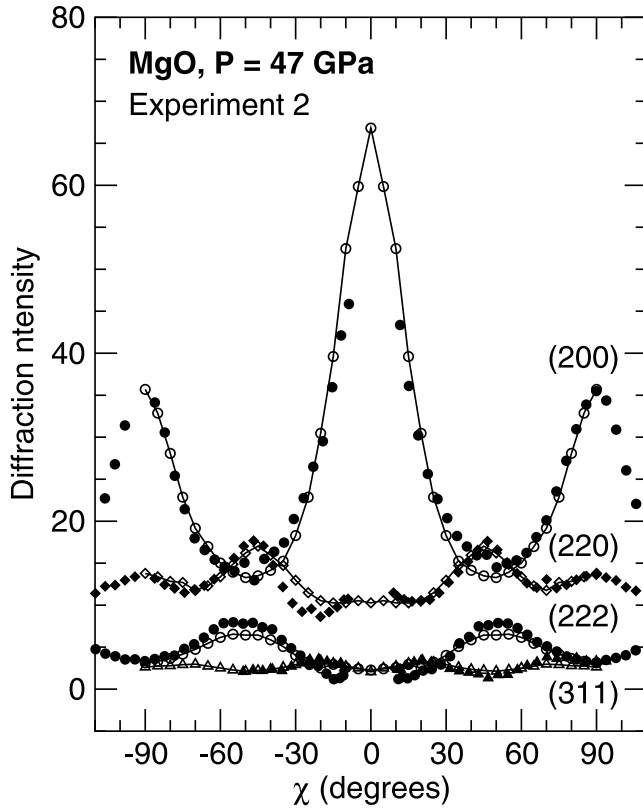
Figure 10. Observed intensities of diffraction and those recalculated from the orientation distribution function (ODF) as a function of the pole distance χ for the peaks (200), (220), (311), and (222), and experiment 2 at $P = 47$ GPa. Closed and open symbols are experimental and recalculated data, respectively. Peaks are labeled on the image.

align parallel or orthogonal to the compression axis. The same relationship is observed in experiment 2.

[35] The intensity variations such as that shown in Figure 9 are used to calculate the ODF of the sample using the Beartex package [*Wenk et al.*, 1998]. Figure 10 shows a comparison between the observed intensities and those recalculated from the ODF for experiment 2 at 47 GPa. The good agreement between these curves gives us confidence in the quality of the fitted ODF.

3.5. Texture Evolution With Pressure

[36] Figure 11 shows the evolution of the texture index in the sample with pressure. In experiment 1, we reach a saturation of the texture index at 2.7 around 20 GPa, while in experiment 2 saturation occurs at 1.3 around 12 GPa.

[37] An efficient way to represent the complete orientation distribution of an axially symmetric texture is the inverse pole figure. An inverse pole figure represents the unique symmetry axis, in our case the compression direction, relative to crystal coordinates. An inverse pole figure displays the symmetry of the crystal, and for cubic MgO a triangle extending from 100 to 110 and 111 is sufficient for a complete representation.

[38] Figure 12 shows inverse pole figures for experiment 1 at 1.9, 5.3, 11.6, and 35.4 GPa. We observe the continuous

development of a single fiber component 100 texture with pressure above 1.9 GPa. At highest pressure, the maximum pole density is 9.12 multiples of random distribution (m.r.d.). Results from experiment 2 are similar, although the magnitude of the preferred orientation is different, with a maximum pole density at highest pressures of 3.07 m.r.d.

4. Discussion

4.1. Pressure Dependence of the Yield Strength

[39] Before heating, the uniaxial stress component in MgO increases with the loading pressure and it saturates around 10 GPa (Figure 6). Other studies of the uniaxial stress component in MgO under pressure include, opposed anvils and Paterson deformation apparatus experiments to 5 GPa [*Bridgman*, 1937; *Weaver and Paterson*, 1969; *Paterson and Weaver*, 1970], multianvil experiments to 8 GPa [*Weidner et al.*, 1994], Drickamer-type press experiments to 20 GPa [*Uchida et al.*, 1996] and diamond anvil cell experiments to 25 GPa [*Kinsland and Bassett*, 1977], between 10 and 40 GPa [*Meade and Jeanloz*, 1988], and to 225 GPa [*Duffy et al.*, 1995]. In all experiments, an increase in the uniaxial stress in the MgO sample with pressure was observed, although the magnitude of the increase differed (e.g., Figure 13).

[40] The maximum uniaxial stress supported by a material is determined by its yield strength; that is $t \leq \sigma_y$, where σ_y is the material yield strength. The uniaxial stress t varies with sample environment and equality holds only if the sample deforms plastically. The yield strength of a polycrystalline material depends on the possible slip systems and their critical resolved shear stress (CRSS), but also on the texture in the sample. Moreover, an increase in the density of dislocations in the sample will result in hardening, that is an increase of the yield stress [*Poirier*, 1985]. It is worth noting that most of the experiments from Figure 13 differ from mechanical tests at constant strain rate which provide a
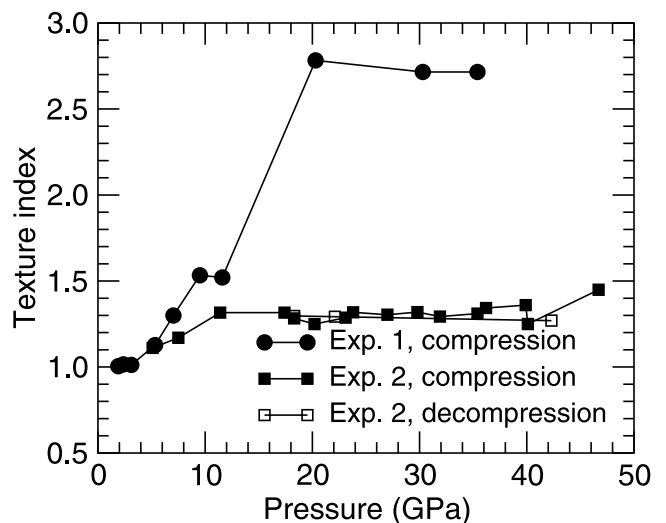

Figure 11. Evolution of texture index of MgO with pressure for experiment 1 upon compression and experiment 2 upon compression and decompression. In experiment 1, we reach a saturation at 2.7 around $P = 20$ GPa, while we reach saturation at 1.3 around $P = 12$ GPa in experiment 2.
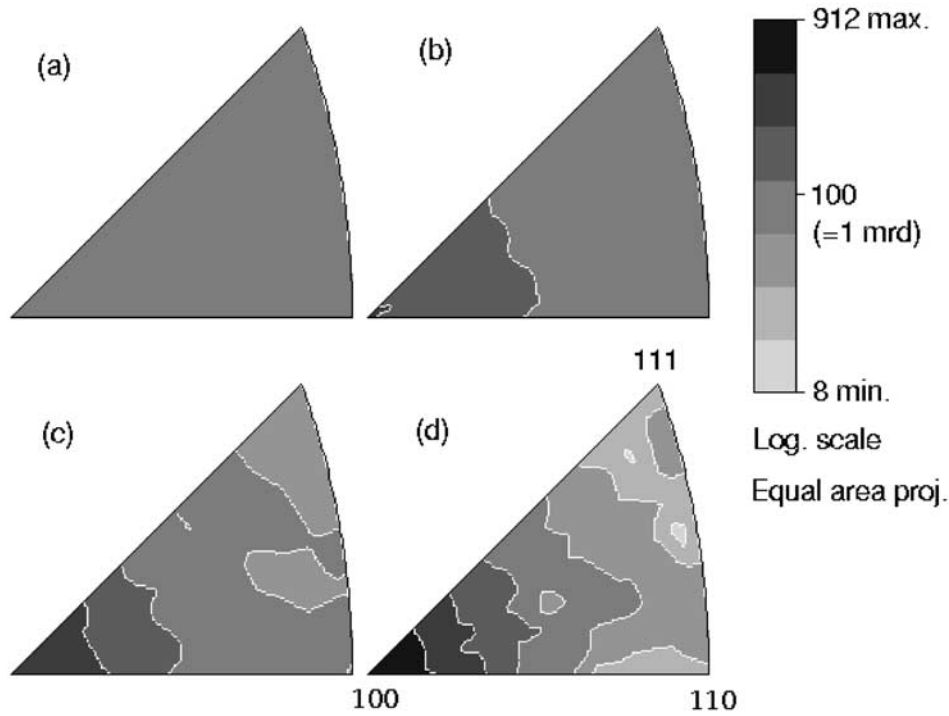
Figure 12. Experimental inverse pole figures illustrating the development of preferred orientation in MgO at 1.9 (a), 5.3 (b), 11.6 (c), and 35.4 (d) GPa for experiment 1. The maximum pole density is 1.0, 2.45, 4.59, and 9.12 multiples of random distribution (m.r.d.) for 1.9, 5.3, 11.6, and 35.4 GPa, respectively.

measure of the yield stress at a given pressure, temperature, and imposed strain rate. In these experiments, strain, strain rate and pressure cannot be decoupled, and therefore, we use a more general definition of the yield stress.

[41] As seen on Figure 13, several experiments, including this one, observe a similar behavior of the uniaxial stress in polycrystalline MgO at low pressure. It increases linearly with pressure with $dt/dP \approx 0.5–0.85$ up to a maximum pressure, function of the experiment, after which it saturates. Results from *Meade and Jeanloz* [1988] and *Duffy et al.* [1995] show a much smoother increase of the uniaxial stress with pressure. Table 3 summarizes the maximum values of uniaxial stress obtained in different experiments on polycrystalline MgO and the pressures at which they were obtained. In these experiments, we obtain a value of t of 8.5($\pm$1) GPa at 10($\pm$1) GPa that is about twice larger that other observations.

[42] Several observations can explain the apparent disagreement between these data. First of all, the yield strength is an upper bound for the uniaxial stress, and it is reached only if the material deforms plastically. For the case of opposed anvil geometry such as the diamond anvil cell, this limit is not always reached between the anvil tips, as shown by finite element modeling [*Merkel et al.*, 2000]. The second effect that has to be taken in consideration is that the yield stress actually depends on the stress history of the polycrystalline sample, and is increased by an augmentation of the dislocation density. In our experi-
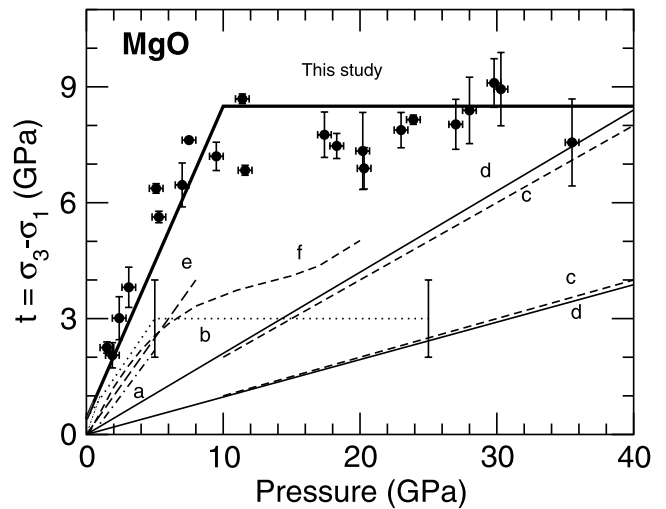

Figure 13. Uniaxial stress component in MgO measured in this study (thick solid line) compared with previous measurements from *Bridgman* [1937] (dot-dashed line, a), *Kinsland and Bassett* [1977] (dotted line, b), *Meade and Jeanloz* [1988] (dashed line c), *Duffy et al.* [1995] (solid line, d), *Weidner et al.* [1994] (long-dashed line, e), and *Uchida et al.* [1996] (dashed line, f). Measurements from *Paterson and Weaver* [1970] fall between just above those of *Bridgman* [1937].

Table 3. Maximum Uniaxial Stress Component and Pressure at Which It Was Obtained in Polycrystalline MgO From Different Experiments[a]

	P	$t = \sigma_3 - \sigma_1$
Paterson and Weaver [1970]	0.5	0.85
Bridgman [1937]	5	2.5
Kinsland and Bassett [1977]	5(±1)	3 ± 1
Weidner et al. [1994]	8	4.5(±1)
Uchida et al. [1996]	20	5
Meade and Jeanloz [1988]	40	8
Meade and Jeanloz [1988]	40	4
Duffy et al. [1995]	100	20
Duffy et al. [1995]	220	>22
This experiment	10(±1)	8.5(±1)

[a] Stress component $t = \sigma_3 - \sigma_1$ and pressure are in GPa.

ments, the uniaxial stress increases drastically up to a pressure of about 10(±1) GPa, after which the increase is much smoother. It can be noticed that this coincides with a change of slope in the curve of the macroscopic deformation of the sample with pressure (Figure 4), changes in the evolution of the texture sharpness with pressure (Figure 11), and the phase transition in the companion Fe sample. Therefore, we infer that there must have been stress hardening in our sample, because of an increase in dislocation density, up to a pressure of about 10(±1) GPa, after which it either stopped or slowed down drastically.

[43] No general conclusion about the evolution of a polycrystalline yield stress of MgO with pressure can be drawn from these experiments. However, for our sample, we observed an uniaxial stress component of about 8.5(±1) GPa at 10(±1) GPa, that implies $\sigma_y \geq 8.5$ GPa at pressures greater than 10 GPa, but this value of σ_y probably includes effects of stress hardening.

4.2. Texture Evolution

[44] The observed texture pattern is comparatively simple with a maximum at [100] in the inverse pole figure; the result can be described as a single fiber component 100 (Figure 12). In experiment 1, the texture increases systematically with pressure and reaches a saturation at 20 GPa with a very high maximal value in the inverse pole figure of over 9 m.r.d. and a corresponding texture index of 2.8. In experiment 2, the texture increases with pressure and reaches saturation at about 12 GPa with a maximum in the inverse pole figure of 3.07 m.r.d. and a texture index of 1.3. During unloading the texture is preserved. Differences between the two experiments are attributed to two factors. The grain size distribution may differ between the two samples, although the average grain size was always less than 1 μm according to visual observations. A small grain size may cause grain boundary sliding and randomization. But the different disposition of the MgO and companion Fe samples might also have this effect. In experiment 1, the MgO and Fe sample were contiguous, unlike experiment 2 where the MgO sample completely surrounded the Fe. This might explain why in experiment 2, the evolution of texture in MgO stopped with the phase transition of the iron from bcc to hcp at 12 GPa.

[45] The (100) texture is similar to that observed in previous compression experiments on MgO [*Meade and Jeanloz*, 1988] but different from other phases with NaCl structure [e.g., halite [*Kern and Braun*, 1973; *Franssen and*

Spiers, 1990], LiF [*Kruger and Bowman*, 1996], PbS [*Siemes and Hennig-Michaeli*, 1985], which generally display two components, a (110) fiber connected with a (100) fiber.

[46] The 100 (cube) texture has been observed after recrystallization, both in extension [*Skrotzki and Welch*, 1983] and compression but our room temperature samples are likely to experience minimal diffusion and show no indication of grain growth. A cube texture could also be expected to develop during compaction if the original fragments were platy parallel to the {100} cleavage. However, there is no evidence that the original grains were platy rather than equiaxed, and the main texture development occurred after compaction. Accordingly, it is reasonable to argue that preferred orientation is due to deformation by slip. In this case the interpretation of deformation mechanisms is aided by comparing the experimental textures with simulated textures based on polycrystal plasticity theory.

4.3. Polycrystal Plasticity

[47] The classic theory of *Taylor* [1938] has been extensively applied to the prediction of plastic deformation of single-phase cubic metallic polycrystals (for reviews, see, e.g., *Kocks et al.* [1998]). This approach assumes homogeneous strain (compatibility) and requires all crystals to deform at the same rate. However, this behavior is not always observed, particularly in low-symmetry minerals where some orientations deform more easily than others to maintain stress equilibrium. In real materials both compatibility and equilibrium need to be maintained, resulting in heterogeneous deformation at the local intracrystalline scale which is still difficult to model numerically and has so far only been attempted for cubic metals with finite element methods [*Mika and Dawson*, 1999]. In recent years, several less sophisticated approaches to model heterogeneous deformation of anisotropic polycrystals have been developed. One is the viscoplastic self-consistent (VPSC) method that is based on regarding each grain as an inclusion embedded in an homogeneous equivalent medium, having the average properties of the polycrystal [*Molinari et al.*, 1987; *Tomé and Canova*, 1998]. This method has been used to predict texture development in various minerals (for a review, see *Wenk* [1999]).

[48] Most relevant for this investigation are simulations of texture development for halite [*Chin*, 1973; *Chin and Mammel*, 1973; *Siemes*, 1974; *Wenk et al.*, 1989] (R. A. Lebensohn et al., Heterogeneous deformation and texture development in halite: Modeling with finite element and self-consistent approaches, submitted to *Tectonophysics*, 2002, hereinafter referred to as Lebensohn et al., submitted manuscript, 2002.). Simulations for halite are rather extraordinary because Taylor and VPSC predicted a very different deformation behavior, particularly for deformation in axial extension. The reason for this difference is that halite, though a mineral with cubic crystal structure, has several slip modes with different relative threshold stresses that vary with temperature and strain rate. In the case of halite at low temperature the $\{110\}\langle 1\bar{1}0\rangle$ slip mode is soft and the $\{100\}\langle 011\rangle$ and $\{111\}\langle 1\bar{1}0\rangle$ slip modes are much harder [*Carter and Heard*, 1970; *Strotzki and Haasen*, 1981]. However, activation of only the soft system does not satisfy the von Mises criterion [*von Mises*, 1928] for an arbitrary

Table 4. Slip Systems, Critical Resolved Shear Stress Ratios (CRSS), and Hardening Parameters Used in the Simulations

Slip System	CRSS ratio	Hardening Parameter
$\{110\}\langle 1\bar{1}0\rangle$	1	2
$\{111\}\langle 1\bar{1}0\rangle$	10	2
$\{100\}\langle 011\rangle$	10	2

deformation. Any combination of soft $\{110\}$ slip systems is unable to accommodate shears of the elementary cube and therefore a combination of hard $\{100\}$ and $\{111\}$ systems become activated. *Chin and Mammel* [1973] discussed the influence of slip systems on texture development in a qualitative way and suggest that $\{110\}$ slip compression axes rotate toward (100), whereas with $\{100\}$ slip they rotate toward (110).

[49] There is little information on deformation mechanisms for MgO. The few studies that exist indicate that slip systems similar to those in halite deformed at low temperature are active, but the plastic anisotropy is even more extreme with $\{110\}\langle 1\bar{1}0\rangle$ being by far the easiest system [*Weaver and Paterson*, 1969; *Paterson and Weaver*, 1970; *Skrotzki and Haasen*, 1984; *Meade and Jeanloz*, 1988; *Foitzik et al.*, 1989]. Based on these results, we assumed a high plastic anisotropy with hard slip modes [i.e., the $\{100\}$ and $\{111\}$ modes being 10 times harder than the $\{110\}$ soft mode] (Table 4).

[50] In order to simulate texture evolution in these deformation experiments on MgO we have used both the Taylor and the self-consistent approaches as implemented in the polycrystal plasticity method of *Lebensohn and Tomé* [1994]. An initial assembly of 2000 randomly oriented grains were deformed in axial compression with 2.5% strain increments to a total von Mises strain of 100%. A linear hardening law was used with a hardening coefficient (stress/strain slope) of 2. The rate-sensitivity of the material was taken as m = 0.05 (stress exponent n = 20) as determined by *Paterson and Weaver* [1970]. Previous studies showed that Taylor and self-consistent simulations give very different results [*Wenk et al.*, 1989] (Lebensohn et al., submited manuscript, 2002). In Taylor simulations the hard $\{100\}$ system is the most active in order to enable compatibility, whereas in self-consistent simulations all deformation occurs on the soft $\{110\}$ system. The resulting textures are different. As in previous simulations Taylor simulations (not shown) show in inverse pole figures a maximum at (110) with a broad shoulder toward (100). Self-consistent simulations (Figure 15) show a single maximum at (100) that can be directly compared with the experimental inverse pole figures in Figure 12.

[51] Some statistical considerations need to be clarified for comparing the experimental and simulated textures to get an independent estimation of strain. We obtained a continuous orientation distribution from discrete orientations in the simulations by entering individual orientations into $5° \times 5° \times 5°$ cells of the ODF. These cells were then smoothed with a Gauss filter. From the smoothed ODF, inverse pole figures were calculated, which are represented as contoured diagrams. The texture strength (expressed as the texture index F_2 and as maximum pole densities) depends on the smoothing, as well as on the number of

orientations [*Matthies and Wagner*, 1996]. In Figure 14 we show the evolution of F_2 with deformation for different conditions. While there is some uncertainty, 2000 grains and a 7.5° Gauss filter reasonably represent the experimental conditions. A texture index between 1.5 and 2 corresponds to a 50–75% von Mises strain.

[52] While the Taylor texture (not shown) is very different from that observed in experiment, the self-consistent texture with a single fiber component at (100) is very similar to that observed in the experiments (Figure 15). In the simulations the maximum increases from 1.8 at 25% strain to 3.0 at 50%, 5.7 at 75% and 10.7 at 100%. $\{110\}\langle 1\bar{1}0\rangle$ is the only active slip system. If the CRSS ratio is reduced from 10 to below 5, harder slip systems become active, and below 2 the self-consistent texture pattern resembles that observed with the Taylor approach. Obviously, deformation that only activates the $\{110\}$ system results in high local incompatibilities, which have to be accommodated by other mechanisms such as grain boundary sliding. Unfortunately we have no information on the microstructures that develop at high pressure in these experiments and therefore this issue cannot be resolved.

[53] We have attempted many conditions and slip systems with both models but, except for self-consistent solutions with $\{110\}\langle 1\bar{1}0\rangle$ models, we could not reproduce the observed texture. We conclude that the $\{110\}$ slip system is the only significantly active slip system in MgO at high pressure and ambient temperature.

4.4. Elastic Anisotropy

[54] Understanding the evolution of elastic anisotropy of deep Earth's minerals with increasing pressure and temperature is of fundamental importance for the understanding of the seismic anisotropy of the Earth's interior [*Mainprice et al.*, 2000]. For cubic materials, it is convenient to express the single crystal anisotropy in terms of the Zener ratio
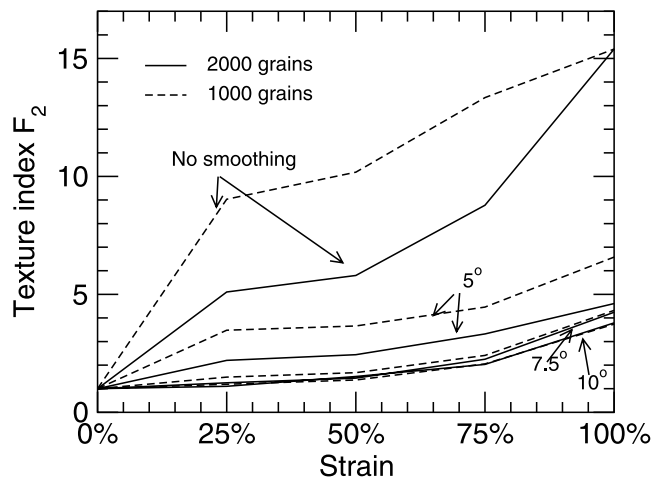

Figure 14. Texture index calculated in the self-consistent simulations as a function a strain for different statistical parameters. Dashed and solid lines are calculations for 1000 and 2000 grains, respectively. For both hypotheses, the ODF was calculated without smoothing or with a 5°, 7.5°, and 10° Gauss filter. Results with 2000 grains and a 7.5° Gauss filter were used for comparison with experimental results.
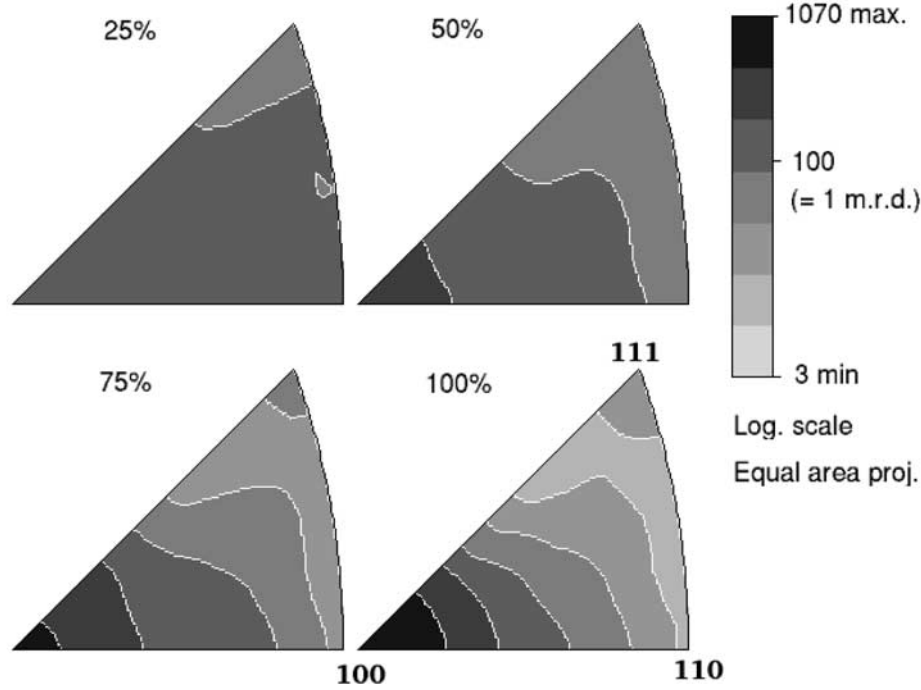
Figure 15. Inverse pole figures illustrating simulated texture development in MgO for 20°C conditions after 25, 50, 75, and 100% strain in axial compression calculated with the viscoplastic self-consistent model.

which is the ratio of the shear moduli in the (100) and (110) planes in the [100] direction,

$$Z = \frac{2C_{44}}{C_{11} - C_{12}} = \frac{2(S_{11} - S_{12})}{S_{44}} \qquad (21)$$

For elastically isotropic materials, we have $Z = 1$. Under the Reuss approximation, Z can be directly measured from radial diffraction experiments, without the use of any assumed bulk property [*Singh et al.*, 1998a; *Duffy et al.*, 1999b; *Merkel et al.*, 2002].

[55] In our experiments, and under the Reuss approximation, Z decreases from its ambient pressure value of 1.546 and saturates at about 0.9 (±0.2) at highest pressures, in agreement with measurements from Brillouin spectroscopy [*Zha et al.*, 2000; *Sinogeikin and Bass*, 2000]. Calculations under the Hill-average provides similar results, increasing the scatter in the data and the anisotropy (Figure 16). Theoretical calculations [*Mehl et al.*, 1986; *Karki et al.*, 1999] predict a continuous decrease in Z with increasing pressures. Observation on the *hkl*-dependence of the lattice strains in conventional diffraction experiments such *Duffy et al.* [1995] and *Speziale et al.* [2001] or radial diffraction experiment [*Uchida et al.*, 1996] require an anisotropy less than 1 at high pressure, with a change in the sign of the anisotropy between 3 and 10 GPa. This is not inconsistent with the results presented here, that show an anisotropy roughly lower than 1 at high pressure, with a change of sign around 8 GPa.

[56] Figure 17 shows the P wave velocity surfaces at 47 GPa for an MgO single crystal and for the polycrystal with the experimental texture from Figure 12 calculated with the

single crystal elastic moduli at this pressure. In the case of the aggregate, the velocity surface displays the symmetry of the sample and is axially symmetric. There are two trends: with increasing pressure the texture increases; however, at
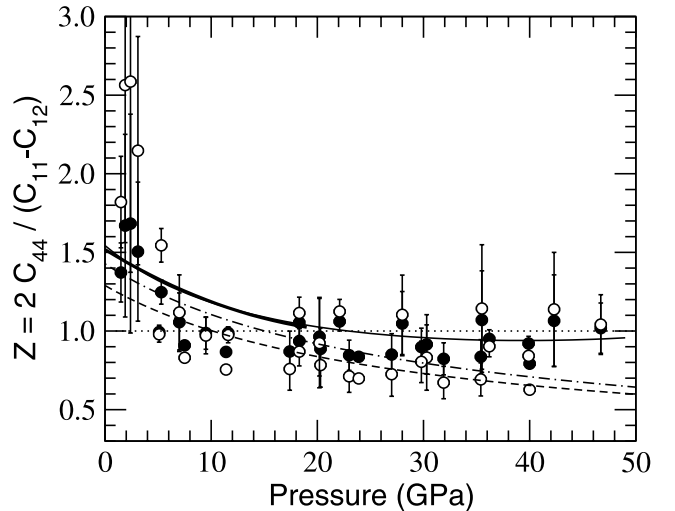

Figure 16. Elastic anisotropy in MgO expressed with the Zener ratio Z. Results from these experiments calculated under the Reuss bound (solid circles) and Hill average (open circles), Brillouin spectroscopy to 19 GPa from *Sinogeikin and Bass* [2000] (thick solid line) and to 55 GPa from *Zha et al.* [2000] (thin solid line), and first principles calculations from *Mehl et al.* [1986] (dotted line) and *Karki et al.* [1999] (dot-dashed line) are indicated.
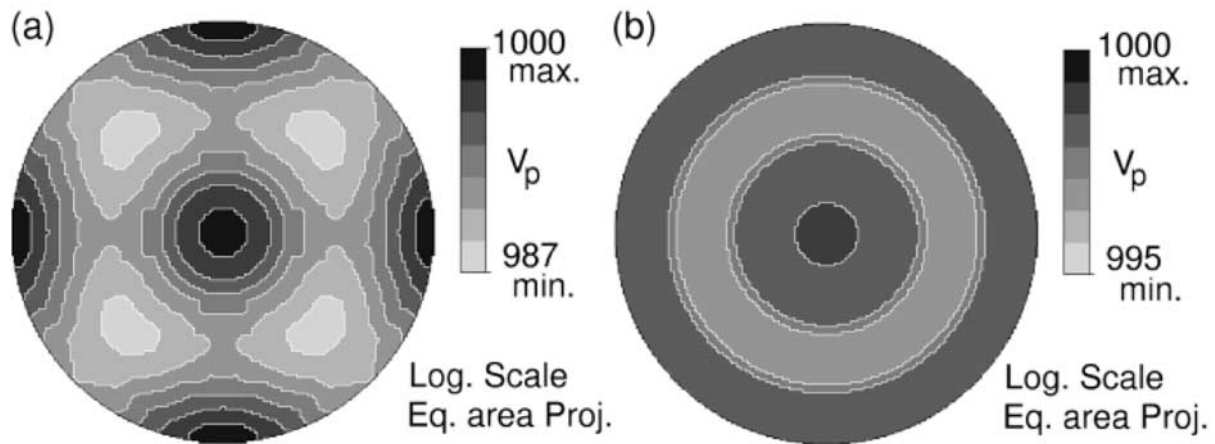
Figure 17. P wave velocity surfaces at 47 GPa. (a) Single crystal velocity surface (b) Velocity surface for the experimental texture measured in this experiment.

the highest pressures the single crystal-elastic anisotropy decreases, resulting in a reduced aggregate anisotropy.

4.5. Implications for the Lower Mantle

[57] Magnesiowüstite is generally believed to be the second most abundant mineral in the Earth's lower mantle. Therefore, understanding the elasticity and rheology of the pure MgO end-member can yield important information about this region of the planet. For cubic materials, single crystal elastic anisotropy and seismic anisotropy can be conveniently related through the anisotropy factor A, defined as

$$A = \frac{2C_{44} + C_{12}}{C_{11}} - 1 \qquad (22)$$

For an isotropic material, A equals zero. The anisotropies of the P, S1, and S2 waves are then given by [e.g., *Karki et al.*, 1997]

$$A_P = \frac{2A}{3}, \quad A_{S1} = -\frac{A}{2} \quad \text{and} \quad A_{S2} = -\frac{3A}{8} \qquad (23)$$

These experiments (consistent with Brillouin measurements [*Zha et al.*, 2000]) indicate a decrease in A from its value of 0.36 at ambient conditions to $-0.05(\pm 0.10)$ at 45 GPa, giving an almost elastically isotropic material at deep mantle pressures. However, zero pressure measurements of the temperature dependence of the elastic moduli of MgO predict an increase of A to 0.77 at 1800 K [*Isaak et al.*, 1989]. Therefore, there is a competing effect of pressure and temperature on the single crystal elastic anisotropy of MgO that could lead to significant anisotropy under lower mantle conditions.

[58] In order to estimate the elastic moduli of MgO at high pressure and temperature, we carry a second-order polynomial extrapolation. We used the pressure and temperatures derivatives from this analysis and *Isaak et al.*'s [1989], respectively. Cross pressure and temperature derivatives have been measured at 8 GPa and between 300 and

1500 K [*Chen et al.*, 1998] but they were not fitted with the same pressure derivatives and are not consistent with this analysis, thus they are not used here. The data fitted ranges between 0 and 47 GPa at 300 K and 300 to 1800 K at ambient pressure. Therefore we feel confident with an extrapolation between 660 km (24 GPa, 1900–2300 K) to about 1660 km depth (70 GPa, 2300–2700 K). This is shown in Figure 18 for the warm and cold geotherms used by *Gillet et al.* [2000]. The anisotropy factor A varies from $0.115(\pm 0.010)$ at 670 km to $0.180(\pm 0.005)$ at 1660 km with a minimum of $0.050(\pm 0.010)$ at 1050 km. Moreover, *Chen et al.* [1998] showed that neglecting temperature derivative of the pressure derivatives underestimates the elastic anisotropy of MgO. Thus, a fairly
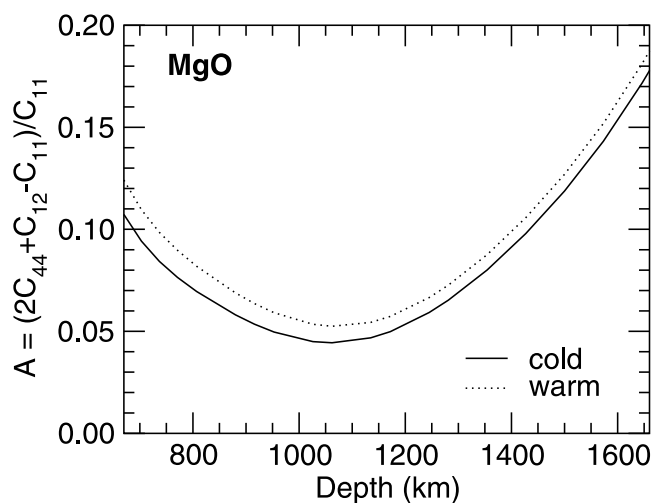

Figure 18. Elastic anisotropy of MgO under the conditions of the upper part of the lower mantle for a cold ($T =$ 1900 K at 670 km, solid line) and a warm ($T =$ 2300 K at 670 km, dotted line) average lower mantle geotherm.

high single crystal elastic anisotropy of MgO under lower mantle conditions is expected.

[59] The influence of iron substitution on the single-crystal elastic anisotropy of (Mg, Fe)O magnesiowüstite under lower mantle conditions remains to be examined directly by experiments. High P-T element partitioning experiments indicate that the amount of Fe present in (Mg, Fe)O in the lower mantle could range from around 10 to 45 mol % FeO [e.g., *Mao et al.*, 1997; *Andrault*, 2001, and references therein]. Ambient conditions measurements of elastic moduli show that A is essentially constant from pure periclase end-member to compositions with ~25% FeO, but then decreases sharply with the FeO end-member being nearly isotropic [*Jacobsen et al.*, 2002]. Thus there are three competing effects of pressure, temperature and composition for the anisotropy of magnesiowüstite. The anisotropy tends to decrease with increasing iron content and increasing pressure, while it increases with temperature. Such conclusions may have to be modified if (Mg, Fe)O undergoes phase transformations at high pressure and temperature [*Mao et al.*, 1996; *Dubrowinsky et al.*, 2000]. This study focused on the high-pressure properties of pure MgO to establish trends for the simple end-member. Additional work, using the techniques presented here, is required to determine the deformation mechanisms and elastic anisotropy of magnesiowüstite under lower mantle conditions.

[60] As for the anisotropy of an aggregate, our deformation experiments on MgO show the development of a very large degree of preferred orientation with increasing pressure. Although we did not measure strain rates, it was observed that 10 to 20 min were needed to stabilize the stress conditions after each increase of load. Therefore, we estimate that the time range of the experiments was about 10^3 s and that our strain rates are on the order of 10^{-3} s^{-1}. Extrapolating our observations to deep Earth conditions (in terms of strain rates and temperature), we infer that a noticable anisotropy could develop in polycrystalline MgO under lower mantle conditions.

[61] The possibility that different slip systems operate at high temperature at these pressures needs to be considered. In NaCl other slip systems do become active as the homologous temperature is approached. In alkali halides there is a high plastic anisotropy at room temperature which decreases with increasing temperature [*Strotzki and Haasen*, 1981; *Strotzki et al.*, 1981]. This may also apply to MgO, though probably not as drastically, so that {110} slip still dominates. At the high temperatures and slow strain rates in the lower mantle, diffusive processes during recovery would alleviate heterogeneity and incompatibility due to activation of a single slip system. Ambient pressure experiments have demonstrated that the CRSS for the {110} and {100} slip systems decrease drastically between ambient temperature and 1500 K, but the plastic anisotropy (i.e., the difference between the CRSS) remains [*Foitzik et al.*, 1989]. Multianvil experiments on MgO at 8 GPa between 300 and 1200° showed a significant temperature dependence of the yield strength with an abrupt change at 500° [*Weidner et al.*, 1994]. This was explained by a change of deformation mechanism from dislocation glide to power law creep with increasing temperature and decreasing deviatoric stress. Deformation mechanisms may

also be influenced by chemical composition. Simple shear experiments at 0.3 GPa and above 1000 K on magnesio-wüstite by *Stretton et al.* [2001] produced texture patterns similar to those observed in fcc metals [e.g., *Hughes et al.*, 2000] suggesting that in this material, and at high temperature, many slip systems are active, including {111}⟨1$\bar{1}$0⟩. Unfortunately simple shear texture patterns of cubic materials are rather insensitive to slip system activity. Therefore, further high P-T investigations of the rheology of MgO and magnesiowüstite of realistic mantle composition, as well as polyphase mixtures, are needed to establish deformation mechanisms and their relevance for the dynamic processes in the deep mantle.

5. Conclusions

[62] We have presented experimental methods to investigate the evolution of single crystal elastic moduli and anisotropy, polycrystal yield strength and deformation mechanisms at pressures relevant to the Earth's deep interior. Measurements are obtained in situ using diamond cell synchrotron X-ray diffraction techniques. In this study, we applied this technique to MgO polycrystals to 47 GPa at room temperature. The results demonstrate the development of a strong texture with increasing pressure in this material. The elastic distortion of the lattice suggests that nonhydrostatic stresses reaches 8.5(±1) GPa and causes deformation of 50–100%. A quantitative comparison of experimental textures and results from polycrystal plasticity simulations suggests that {110}⟨1$\bar{1}$0⟩ is the only significantly active slip system at the conditions of these experiments.

[63] Although we may included effects of stress hardening because of an increased dislocation density, analysis of the low temperature yield strength suggests an increase from the ambient pressure value of 0.4 GPa to a minimum of 8.5(±1) GPa at 10(±1) GPa and higher pressures. The single crystal elastic anisotropy tends to decrease with pressure, with the material becoming almost elastically isotropic at pressures of about 50 GPa. However, a competing effect of pressure and temperature results in single crystal elastic anisotropy of MgO at lower mantle conditions. The anisotropy factor A decreases from 0.115(±0.010) at 670 km depth to 0.050(±0.010) at 1050 km depth and then increases again to 0.180(±0.005) at 1660 km depth.

[64] With this study we show the feasibility of the experimental study of deformation mechanisms, single crystal and polycrystal elastic moduli and anisotropy, as well as polycrystal strength at deep mantle pressures. This approach can now be extended to study the behavior at both high pressure and temperature. The same technique can also be used to study other mantle component, including the influence of iron substitution in (Mg, Fe)O magnesiowüstite and (Mg, Fe)SiO$_3$ perovskite, as well as deformation of composites of the two minerals. Such experiments will provide information about deformation mechanisms and mechanical properties of minerals in the deep Earth that are a prerequisite for realistic geodynamic models.

References

Andrault, D., Evaluation of (Mg, Fe) partitioning between silicate perovskite and magnesiowüstite up to 120 GPa and 2300 K, *J. Geophys. Res.*, *106*, 2079–2087, 2001.

Bridgman, P. W., Shearing phenomena at high pressures, particularly in inorganic compounds, *Proc. Am. Acad. Sci.*, *71*, 387–460, 1937.

Carter, N. L., and H. C. Heard, Temperature and rate dependent deformation of halite, *Am. J. Sci.*, *269*, 193–249, 1970.

Chastel, Y. B., P. R. Dawson, H. R. Wenk, and K. Bennett, Anisotropic convection with implications for the upper mantle, *J. Geophys. Res.*, *98*, 17,757–17,771, 1993.

Chen, G., R. C. Liebermann, and D. J. Weidner, Elasticity of single crystal MgO to 8 gigapascals and 1600 kelvins, *Science*, *280*, 1913–1916, 1998.

Chin, G. Y., A theoretical examination of the plastic deformation of ionic crystals, I, Maximum work analysis for slip on {110}⟨110⟩ and {100}⟨110⟩ systems, *Metall. Trans.*, *4*, 329–333, 1973.

Chin, G. Y., and W. L. Mammel, A theoretical examination of the plastic deformation of ionic crystals, II, Analysis of uniaxial deformation and axisymmetric flow for slip on {110}⟨110⟩ and {100}⟨110⟩ systems, *Metall. Trans.*, *4*, 335–340, 1973.

Cynn, H. C., and C. S. Yoo, Elasticity of tantalum to 105 GPa using a stress and angle-resolved X-ray diffraction, in *Science and Technology of High Pressure*, edited by M. Manghnani, W. Nellis, and M. F. Nicol, pp. 432–435, Univ. Press (India), 2000.

Davies, G. F., and A. M. Dziewonski, Homogeneity and constitution of the Earth's lower mantle and outer core, *Phys. Earth Planet. Inter.*, *10*, 336–343, 1975.

Dewaele, A., G. Fiquet, D. Andrault, and D. Häusermann, P-V-T equation of state of periclase from synchrotron radiation measurements, *J. Geophys. Res.*, *105*, 2869–2877, 2000.

Dubrowinsky, L. S., N. A. Dubrovinskaia, S. K. Saxena, H. Annersten, E. Hålenius, H. Harryson, F. Tutti, S. Rekhi, and T. LeBihan, Stability of ferropericlase in the lower mantle, *Science*, *289*, 430–432, 2000.

Duffy, T. S., and T. J. Ahrens, Sound velocities at high pressure and temperature and their geophysical implications, *J. Geophys. Res.*, *97*, 4503–4520, 1992.

Duffy, T. S., R. J. Hemley, and H. K. Mao, Equation of state and shear strength at multimegabar pressures: Magnesium oxide to 227 GPa, *Phys. Rev. Lett.*, *74*, 1371–1374, 1995.

Duffy, T. S., G. Shen, D. L. Heinz, J. Shu, Y. Ma, H. K. Mao, R. J. Hemley, and A. K. Singh, Lattice strains in gold and rhenium under non-hydrostatic compression to 37 GPa, *Phys. Rev. B*, *60*, 1–10, 1999a.

Duffy, T. S., G. Shen, J. Shu, H. K. Mao, R. J. Hemley, and A. K. Singh, Elasticity, shear strength and equation of state of molybdenum and gold from X-ray diffraction under nonhydrostatic compression to 24 GPa, *J. Appl. Phys.*, *86*, 1–8, 1999b.

Fiquet, G., Mineral phases of the earth's mantle, *Z. Krystallogr.*, *216*, 248–271, 2001.

Foitzik, A., W. Skrotzki, and P. Haasen, Correlation between microstructure, dislocation dissociation and plastic anisotropy in ionic crystals, *Mater. Sci. Eng.*, *A113*, 399–407, 1989.

Franssen, R. C. M. W., and C. J. Spiers, Deformation of polycrystalline salt in compression and in shear at 250–350°C, in *Deformation Mechanisms. Rheology and Tectonics*, *Geol. Soc. London, Spec. Publ.*, vol. 45, edited by R. J. Knipe and E. H. Rutter, pp. 201–213, 1990.

Gillet, Ph., I. Daniel, F. Guyot, J. Matas, and J. C. Chervin, A thermodynamical model for MgSiO₃-perovskite derived from pressure, temperature and volume dependence of Raman mode frequencies, *Phys. Earth Planet. Inter.*, *117*, 361–384, 2000.

Gnäupel-Herold, T., P. C. Brand, and H. J. Prask, The calculation of single crystal elastic constants for cubic crystal symmetry from powder diffraction data, *J. Appl. Crystallogr.*, *31*, 929–935, 1998.

Hammersley, A. P., Fit2d: V9.129 reference manual v3.1, *Internal Rep. ESRF98HA01*, ESRF, 1998.

Heidelbach, F., C. Riekel, and H. R. Wenk, Quantitative texture analysis of small domains with synchrotron radiation X-rays, *J. Appl. Crystallogr.*, *32*, 841–849, 1999.

Heinz, D. L., and R. Jeanloz, Temperature measurement in the laser heated diamond anvil cell, in *High Pressure Researches in Mineral Physics*, edited by M. H. Manghnanin and Y. Syono, pp. 113–127, AGU, Washington, D. C., 1987.

Howard, C. J., and E. H. Kisi, Measurement of single-crystal elastic constants by neutron diffraction from polycrystals, *J. Appl. Crystallogr.*, *32*, 624–633, 1999.

Hughes, D. A., R. A. Lebensohn, H. R. Wenk, and A. Kumar, Stacking fault energy and microstructure effects on torsion texture evolution, *Proc. R. Soc. London, Ser. A*, *456*, 921–953, 2000.

Isaak, D. G., O. L. Anderson, and T. Goto, Measured elastic moduli of single crystal MgO up to 1800 K, *Phys. Chem. Miner.*, *16*, 704–713, 1989.

Isaak, D. G., R. E. Cohen, and M. E. Mehl, Calculated elastic constants and thermal properties of MgO at high pressures and temperatures, *J. Geophys. Res.*, *95*, 7055–7067, 1990.

Jacobsen, S. D., H. J. Reichmann, H. A. Spetzler, S. J. Mackwell, J. R. Smyth, R. J. Angel, and C. A. McCammon, Structure and elasticity of single-crystal (Mg, Fe)O and a new method of generating shear waves for gigahertz ultrasonic interferometry, *J. Geophys. Res.*, *107*, 2037, doi:10.1029/2001JB000490, 2002.

Karato, S., and P. Li, Diffusion creep in perovskite: Implications for the rheology of the lower mantle, *Science*, *255*, 1238–1240, 1992.

Karki, B. B., L. Stixrude, S. J. Clark, M. C. Warren, G. J. Ackland, and J. Crain, Structure and elasticity of MgO at high pressure, *Am. Mineral.*, *82*, 51–60, 1997.

Karki, B. B., R. M. Wentzcovitch, S. de Gironcoli, and S. Baroni, First-principles determination of elastic anisotropy and wave velocities of MgO at lower mantle conditions, *Science*, *286*, 1705–1707, 1999.

Kern, H., and G. Braun, Deformation und gefügeregelung von steinsalz im temperaturbereich 20–200 C, *Contrib. Mineral. Petrol.*, *40*, 169–181, 1973.

Kinsland, G. L., and W. A. Bassett, Strength of MgO and NaCl polycrystals to confining pressures of 250 kbar at 25 C, *J. Appl. Phys.*, *48*, 978–984, 1977.

Kocks, F. U., C. Tomé, and H. R. Wenk, *Texture and Anisotropy: Preferred Orientations and their Effects on Material Properties*, Cambridge Univ. Press, New York, 1998.

Kruger, K. L., and K. J. Bowman, A comparison of texture development in plane strain and axisymmetrically compressed lithium fluoride, in *Proceedings ICOTOM*, *11*, pp. 998–1003, 1996.

Lebensohn, R. A., and C. N. Tomé, A self-consistent visco-plastic model: Calculation of rolling textures of anisotropic materials, *Mater. Sci. Eng., A*, *175*, 71–82, 1994.

Li, P., S. Karato, and Z. Wang, High-temperature creep in fine-grained polycrystalline CaTiO₃, an analogue material of (Mg, Fe)SiO₃ perovskite, *Phys. Earth Planet. Inter.*, *95*, 19–36, 1996.

Mainprice, D., G. Barruol, and W. Ben Ismäuml;l, The seismic anisotropy of the earth's mantle: From single crystal to polycrystal, in *Earth's Deep Interior. Mineral Physics and Tomography. From the Atomic to the Global Scale*, edited by S. Karato et al., pp. 237–264, AGU, Washington, D. C., 2000.

Mao, H. K., J. Shu, Y. Fei, J. Hu, and R. J. Hemley, The wüstite enigma, *Phys. Earth Planet. Inter.*, *96*, 135–145, 1996.

Mao, H. K., G. Shen, and R. J. Hemley, Multivariable dependence of Fe-Mg partitioning in the lower mantle, *Science*, *278*, 2098–2100, 1997.

Mao, H. K., J. Shu, G. Shen, R. J. Hemley, B. Li, and A. K. Singh, Elasticity and rheology of iron above 220 GPa and the nature of the earth's inner core, *Nature*, *396*, 741–743, (Correction, *Nature*, *399*, 280, 1999), 1998.

Matthies, S., and F. Wagner, On a 1/n law in texture related single orientation analysis, *Phys. Status Solidi*, *196*, 1996.

Matthies, S., S. Merkel, H. R. Wenk, R. J. Hemley, and H. K. Mao, Effects of texture on the high pressure elasticity of iron from X-ray diffraction, *Earth Planet. Sci. Lett.*, *194*, 201–212, 2001.

Meade, C., and R. Jeanloz, Yield strength of MgO to 40 GPa, *J. Geophys. Res.*, *93*, 3261–3269, 1988.

Meade, C., P. G. Silver, and S. Kanshima, Laboratory and seismological observations of lower mantle isotropy, *Geophys. Res. Lett.*, *22*, 1293–1296, 1995.

Mehl, M. J., R. J. Hemley, and L. L. Boyer, Potential-induced breathing model for the elastic moduli and high-pressure behavior of the cubic alkaline-earth oxides, *Phys. Rev. B*, *33*, 8685–8696, 1986.

Merkel, S., R. J. Hemley, H. K. Mao, and D. M. Teter, Finite element modeling and ab-initio calculations of megabar stresses in the diamond anvil cell, in *Science and Technology of High Pressure Research*, edited by M. Manghnani, W. J. Nellis, and M. F. Nicol, pp. 68–73, Univ. Press (India), 2000.

Merkel, S., A. P. Jephcoat, J. Shu, H. K. Mao, Ph. Gillet, and R. J. Hemley, Equation of state, elasticity and shear strength of pyrite under high pressure, *Phys. Chem. Miner.*, *29*, 1–9, 2002.

Mika, D. P., and P. R. Dawson, Polycrystal plasticity modeling of intra-crystalline boundary textures, *Acta Mater.*, *47*, 1355–1369, 1999.

Molinari, A., G. R. Canova, and S. Ahzi, A self-consistent approach of the large deformation polycrystal viscoplasticity, *Acta Metall.*, *35*, 2983–2994, 1987.

Paterson, M. S., and C. W. Weaver, Deformation of polycrystalline MgO under pressure, *J. Am. Ceram. Soc.*, 53, 463–471, 1970.

Poirier, J. P., *Creep of Crystals*, Cambridge Univ. Press, New York, 1985.

Poirier, J. P., and G. D. Price, Primary slip system of ϵ-iron and anisotropy of the Earth's inner core, *Phys. Earth Planet. Inter.*, 110, 147–156, 1999.

Reichmann, H. J., R. J. Angel, H. Spetzler, and W. A. Bassett, Utrasonic interferometry and X-ray measurements on MgO in a new diamond anvil cell, *Am. Mineral.*, 83, 1357–1360, 1998.

Shen, A. H., H. J. Reichmann, G. Shen, R. J. Angel, W. A. Bassett, and H. Spetzler, GHz ultrasonic interferometry in a diamond anvil cell: P-wave velocities in periclase to 4.4 GPa and 207°C, in *Properties of Earth and Planetary Materials at High Pressure and Temperature*, edited by M. Manghnani and T. Yagi, pp. 71–77, AGU, Washington, D. C., 1998.

Siemes, H., Anwendung der taylor theorie auf die regelung von kubischen mineralen, *Contrib. Mineral. Petrol.*, 43, 149–157, 1974.

Siemes, H., and V. Hennig-Michaeli, Ore minerals, in *Preferred Orientations in Deformed Metals and Rocks: An Introduction to Modern Texture Analysis*, edited by H. R. Wenk, pp. 335–360, Academic, San Diego, Calif., 1985.

Singh, A. K., The lattice strains in a specimen (cubic system) compressed nonhydrostatically in an opposed anvil device, *J. Appl. Phys.*, 73, 4278–4286, 1993.

Singh, A. K., C. Balasingh, H. K. Mao, R. J. Hemley, and J. Shu, Analysis of lattice strains measured under non-hydrostatic pressure, *J. Appl. Phys.*, 83, 7567–7575, 1998a.

Singh, A. K., H. K. Mao, J. Shu, and R. J. Hemley, Estimation of single crystal elastic moduli from polycrystalline X-ray diffraction at high pressure: Applications to FeO and iron, *Phys. Rev. Lett.*, 80, 2157–2160, 1998b.

Sinogeikin, S. V., and J. D. Bass, Single crystal elasticity of pyrope and MgO to 20 GPa by brillouin spectroscopy scattering in the diamond cell, *Phys. Earth Planet. Inter.*, 120, 43–62, 2000.

Sinogeikin, S. V., J. M. Jackson, B. O'Neil, J. W. Palko, and J. D. Bass, Compact high pressure cell for brillouin scattering measurements, *Rev. Sci. Instrum.*, 71, 201–206, 2000.

Skrotzki, W., and P. Haasen, Hardening mechanisms of ionic crystals on {110} and {100} slip planes, *J. Phys. (Paris)*, 42, 119–148, 1981.

Skrotzki, W., and P. Haasen, Plastic hardening of polycrystalline halides, in *Materials Research: Deformation of Ceramic Materials II*, edited by R. Tressler and R. Bradt, vol. 18, pp. 429–444, Plenum, New York, 1984.

Skrotzki, W., and P. Welch, Development of texture and microstructure in extruded ionic polycrystalline aggregates, *Tectonophysics*, 99, 47–61, 1983.

Skrotzki, W., G. Frommeyer, and P. Haasen, Plasticity of polycrystalline ionic solids, *Phys. Status Solidi*, A66, 219, 1981.

Speziale, S., C. S. Zha, T. S. Duffy, R. J. Hemley, and H. K. Mao, Quasi-hydrostatic compression of magnesium oxide to 52 GPa: Implications for the pressure-volume-temperature equation of state, *J. Geophys. Res.*, 106, 515–528, 2001.

Stixrude, L., Elasticity of mantle phases at high pressure and temperature, in *Earth's Deep Interior. Mineral Physics and Tomography. From the Atomic to the Global Scale*, edited by S. Karato et al., pp. 201–213, AGU, Washington, D. C., 2000.

Stretton, I., F. Heidelbach, S. Mackwell, and F. Langenhorst, Dislocation creep of magnesiowüstite ($Mg_{.8}Fe_{0.2O}$), *Earth Planet. Sci. Lett.*, 94, 229–240, 2001.

Taylor, G. I., Plastic strain in metals, *J. Inst. Met.*, 62, 307–324, 1938.

Tomé, C. N., and G. R. Canova, in *Texture and Anisotropy. Preferred Orientations in Polycrystals and Their Effect on Materials Properties*, edited by U. F. Kocks, C. N. Tomé, and H. R. Wenk, chap. 11, pp. 561–595, Cambridge Univ. Press, New York, 1998.

Tullis, T. E., and J. Tullis, Experimental rock deformation techniques, in *Mineral and Rock Deformations: Laboratories Studies*, edited by B. E. Hobbs and H. C. Heard, pp. 297–324, AGU, Washington, D. C., 1986.

Uchida, T., N. Funamori, T. Ohtani, and T. Yagi, Differential stress of MgO and Mg_2SiO_4 under uniaxial stress field: Variation with pressure, temperature, and phase transition, in *High Pressure Science and Technology*, edited by W. A. Trzeciatowski, pp. 183–185, World Sci., River Edge, N. J., 1996.

von Mises, R., Mechanik der plastischen Formänderung von Kristallen, *Z. Angew. Math. Mech.*, 8, 161–185, 1928.

Weaver, C. W., and M. S. Paterson, Deformation of cube-oriented MgO crystals under pressure, *J. Am. Ceram. Soc.*, 52, 293–302, 1969.

Weidner, D. J., Y. Wang, and M. T. Vaughan, Yield strength at high pressure and temperature, *Geophys. Res. Lett.*, 21, 753–756, 1994.

Wenk, H. R., A voyage through the deformed earth with the self-consistent model, *Model. Simul. Mater. Sci. Eng.*, 7, 699–722, 1999.

Wenk, H. R., G. R. Canova, A. Molinari, and H. Mecking, Texture development in halite: Comparison of Taylor model and self-consistent theory, *Acta Metall.*, 37, 2017–2029, 1989.

Wenk, H. R., S. Matthies, J. Donovan, and D. Chateigner, Beartex: A windows-based program system for quantitative texture analysis, *J. Appl. Crystallogr.*, 31, 262–269, 1998.

Wenk, H. R., S. Matthies, R. J. Hemley, H. K. Mao, and J. Shu, The plastic deformation of iron at pressures of the Earth's inner core, *Nature*, 405, 1044–1047, 2000.

Yoneda, A., Pressure derivatives of elastic constants of single crystal MgO and $MgAl_2O_4$, *J. Phys. Earth*, 38, 19–55, 1990.

Zha, C. S., H. K. Mao, and R. J. Hemley, Elasticity of MgO and a primary pressure scale to 55 GPa, *Proc. Natl. Acad. Sci. U.S.A.*, 97, 13,494–13,499, 2000.

————————————

Ph. Gillet and S. Merkel, Laboratoire des sciences de la Terre, École normale supérieure de Lyon, 46 allée d'Italie, 69364 Lyon, Cedex 07, France. (sebastien.merkel@ens-lyon.fr)

R. J. Hemley, H. K. Mao, and J. Shu, Geophysical Laboratory, Carnegie Institution of Washington, 5251 Broad Branch Rd., NW, Washington, D. C. 20015, USA.

G. Shen, Consortium for Advanced Radiation Sources, University of Chicago and Advanced Photon Source, Argonne National Laboratory, 9700 South Cass Avenue, Argonne, IL 60439, USA.

H. R. Wenk, Department of Earth and Planetary Science, University of California, Berkeley, CA 94720, USA.